Preprint of B. Davis, J.E. Shepherd and R. Mevel, Numerical modeling of gaseous n-hexane autoignition in an ASTM-E659 apparatus. Fuel 405 (2026) 136691.
See https://doi.org/10.1016/j.fuel.2025.136691 for published version.

Graphical Abstract

Numerical Modeling of Gaseous n-Hexane Autoignition in an ASTM-E659 Apparatus

Branson Davis, Joseph Shepherd, Rémy Mével

Fluid motion and chemical reaction during ASTM E-659 auto-ignition testing in a 500 mL flask open to atmosphere and filled with hot (520 K) stoichiometric nC6H14-air mixture

Pre-ignition phase, buoyancy driven flow, and creation of a toroidal ignition kernel.

First stage of self-ignition by low temperature, “cool flame” reactions, gas motion out of flask due to thermal expansion

Second stage of self-ignition by high temperature reactions and flame propagation throughout flask.

Highlights

Numerical Modeling of Gaseous n-Hexane Autoignition in an ASTM-E659 Apparatus

Branson Davis, Joseph Shepherd, Rémy Mével

- Three-dimensional, computational fluid dynamics simulations are reported for the autoignition and flame propagation of nC_6H_{14}-air mixtures in an ASTM-E659 apparatus.
- A detailed chemical kinetics model is used to demonstrate a two-stage ignition behavior with distinct low- and high-temperature reaction pathways.
- Ignition occurs while the fuel is stratified in the flask, occurring in a fuel rich location.
- An asymmetric ring-like kernel forms near the hot walls, driven by the initial mixing transient and intrusion of cold gas through the center of the flask.
- The resultant flame propagates out of the flask, burning the fuel expelled by gas expansion.

Numerical Modeling of Gaseous n-Hexane Autoignition in an ASTM-E659 Apparatus

Branson Davis[a], Joseph Shepherd[a], Rémy Mével[b]

[a] *California Institute of Technology, Pasadena, 91125, CA, USA*
[b] *Zhejiang University, Hangzhou, China*

Abstract

Numerical simulation of three-dimensional motion, molecular transport, and chemical reactions is reported for gaseous nC_6H_{14} autoignition in an ASTM-E659 apparatus, a 500 mL round-bottom, heated flask filled with hot air and the top open to the atmosphere. The injected fuel is heavier than air, initially flows to the bottom of the flask and diffuses up over time as a stratified layer. Inflow of cold air from the open end of the flask penetrates downward and mixes with the flask contents. The inflow and convection due to the heated flask are observed to create a vortical motion. Chemical reactions were modeled using a reduced kinetic mechanism suitable for low-temperature oxidation of nC_6H_{14}. Reaction begins slowly and more substantially near the walls where the local gas temperature is hottest. A ring-like ignition kernel forms followed by a localized two-stage ignition event in a rich fuel/air mixture. Critical reaction pathways were identified for both ignition stages. The resultant flame propagation, which is inhibited towards the bottom by lack of oxygen molecules in this region of the flask, convects upwards, chasing unburnt fuel expelled from the flask due to gas expansion from the ignition event itself. Implications are discussed for refinement of autoignition testing.

Keywords: Autoignition, ASTM E-659, Self heating, Safety

1. Introduction

Autoignition temperature (AIT) is a critical parameter widely used [1, 2, 3] to evaluate the potential ignition hazards of combustible gases and liquids

Email address: joseph.e.shepherd@caltech.edu (Joseph Shepherd)

in hot atmospheres. Extensive tabulations [4, 5] are available of test results based on standardized methods such as ASTM-E659 [6], EN 14522 and DIN 51794 [7]. Our recent studies [8, 9] show a variety of ignition behaviors and various comparative studies [10, 11] have demonstrated that the results are specific to the measurement technique.

Various other studies have also investigated the influence of natural convection, both reactive [12, 13, 14, 15, 16, 17, 18] and nonreactive [19], on the temperature distribution and ignition behavior in closed spherical and cylindrical vessels with initially homogeneous mixtures. A review of the previous work can be found in in Davis et al. [20]. Natural convection driven by exothermic chemical reaction was found to induce the formation of a toroidal vortex, gas moves upward through the center and sinks downward the outer surface. Recent work by Davis et al. [20] found that the open vessel design and fuel dispersion inside the flask during an E659 standardized test contributed significant non-reactive convective effects not previously considered. Intrusion of cold gas through the top of the flask drives a counter-rotating vortex compared to what has been seen for idealized vessels, where gas rises near the heated walls and sinks through the center.

This study extends the results presented by Davis et al. [20] on the non-reactive mixing behavior of gaseous nC6H14 in an open vessel compliant with the E659 standard to include chemical reactions. A detailed kinetic mechanism was reduced in size to enable reacting simulations. The reaction mechanism included both low- and high-temperature reaction pathways that reproduce both quantitative and qualitative features of ignition. The ignition process in this configuration proceeds through several distinct stages that will be analyzed in detail: i) fuel dispersion and stratification following injection, ii) a pre-ignition "cooking phase" marked by slow low-temperature reactions, iii) a multi-stage ignition event driven by coupled chemical-thermal runaway, iv) transition to high-temperature reactions with subsequent flame propagation shaped by the evolving composition and flow field. While the present simulations assume an initially gaseous fuel distribution, the actual ASTM-E659 test involves a two-phase jet injection, including droplet breakup, vaporization, and liquid–wall interactions, which are not considered in the current analysis.

2. Numerical methods

2.1. Geometric model and meshing

For our study, the experimental setup constructed by [8, 21] following the ASTM-E659-24 [6] standard and numerically modeled by Davis et al. [20] was used for reacting flow simulation. The portion of the experiment being simulated is a uniformly-heated, 500 mL, round-bottom pyrex flask with the top open to the atmosphere. The details of the ASTM E-659 apparatus and the geometrical model of the flask are described in Davis et al. [20], Fouchier and Shepherd [9]. A three-dimensional numerical mesh of the interior of the flask was created using the OpenFOAM tool, snappyHexMesh with priority given to uniform hexahedral cells. The grid-independence of the solution is discussed in 3.1. Statistically converged results were obtained using a total of 10^6 cells with a nominal dimension of 600 μm. A rectangular region with open boundaries was placed above the opening of the flask. This models the exchange of gas between the flask and the surrounding atmosphere that occurs during the ASTM E-659 test.

2.2. Governing equations

The numerical model is based on the variable-density, Navier-Stokes equations with a non-Boussinesq buoyancy force in the momentum equation. Realistic temperature- and species-dependent transport properties were used in the momentum, energy and species equations.

$$\frac{\partial \rho}{\partial t} + \nabla \cdot (\rho \mathbf{u}) = 0\,, \tag{1}$$

$$\frac{\partial}{\partial t}(\rho \mathbf{u}) + \nabla \cdot (\rho \mathbf{u}\mathbf{u} + p\mathbf{I}) = \nabla \cdot \tau + \rho \mathbf{g}\,, \tag{2}$$

$$\frac{\partial}{\partial t}(\rho Y_i) \;+\; \nabla \;\cdot\; (\rho Y_i \mathbf{u}) \;\;=\;\; -\nabla \;\cdot\; (\rho Y_i \mathbf{V}_i) \;+\; \dot{\Omega}_i \quad i \;\;=\;\; 1, 2, \ldots, N\,, \tag{3}$$

$$c_P \frac{\partial}{\partial t}(\rho T) + c_P \nabla \cdot (\rho \mathbf{u} T) = \\ - \nabla \cdot (\lambda \nabla T) - \rho \nabla T \cdot \sum_{i=1}^{N} c_{P,i} Y_i \mathbf{V}_i - \sum_{i=1}^{N} h_i \dot{\Omega}_i\,. \tag{4}$$

The symbols are: t time; ρ mixture density; p pressure, u velocity; g gravitational acceleration; T temperature, c_P specific heat capacity at constant pressure; λ mixture thermal conductivity, Y_i species mass fraction, $\mathbf{V}$ diffusion velocity, $\dot{\Omega}_i$ net volumetic mass production rate of species i; h specific enthalpy; and τ the viscous stress tensor:

$$\tau = \mu(\nabla \mathbf{u} + (\nabla \mathbf{u})^T) - \frac{2}{3}\mu(\nabla \cdot \mathbf{u})\mathbf{I}\,, \tag{5}$$

$\mathbf{I}$ is the identity matrix. The total number of species is N and the density of the mixture was computed from the local presssure, temperature, and composition using $\rho = p/RT$.

Diffusion velocities are calculated using the conventional approximate formulation:

$$\mathbf{V_i} = -\frac{D_i}{Y_i}\nabla Y_i - \frac{D_i \Theta_i}{X_i}\frac{1}{T}\nabla T\,, \tag{6}$$

including a contribution by thermodiffusion (Soret effect); X_i are the species mole fractions, Θ_i is the thermodiffusion ratio. Mixture-averaged diffusion coefficients are calculated using the approximate formulation of Curtiss and Hirschfelder [22]

$$D_i = \frac{1 - Y_i}{\sum_{j \neq i}^{N} \frac{X_i}{\Gamma_{ji}}}\,, \tag{7}$$

where Γ_{ji} are the binary diffusion coefficients. The correction of Coffee and Heimerl [23] is applied to $\mathbf{V}_i$ in Eqs (3) and (4) as:

$$\mathbf{V}_i^C = \mathbf{V}_i + \mathbf{V}_C\ . \tag{8}$$

Standard CFD methods using segregated algorithms are typically unsuitable for reacting flow problems involving large chemical mechanisms due to high stiffness and nonlinearities of the species and energy transport equations. Operator-splitting techniques can instead be used to separate the terms associated with nonstiff processes (convective and diffusive transport) from those associated with stiff processes (chemical reactions). Eqs (1)-(4) were numerically integrated in the OpenFOAM framework in the open-source *laminarBuoyantPimpleSMOKE* solver which uses the pressure implicit with splitting of operators (PISO) algorithm and the Strang splitting scheme [24, 25]. Second-order central differencing was employed to compute the spatial derivatives. More information about the solver can be found in Cuoci et al. [26, 27].

2.3. Kinetic modeling

Autoignition experiments for liquid hydrocarbon fuels often take place at low temperatures (< 800 K) as shown in Martin and Shepherd [8] and Fouchier and Shepherd [9]. It is well understood that the chemical reaction pathways for heavy n-alkane oxidation in this temperature regime differ from those at more elevated temperatures (> 1000 K) as evident from the observed "negative temperature coefficient" (NTC) region as shown in Westbrook and Dryer [28] and Battin-Leclerc [29] along with many other studies. Thus, both high- and low-temperature reaction pathways must be included when simulating such an environment. For these purposes, the *CaltechMech* full mechanism [30] was selected for creating a reduced mechanism to use in multidimensional reacting flow studies. The *CaltechMech* mechanism was validated against extensive experimental data including laminar premixed flames, laminar diffusion flames, and homogeneous reactors for a wide range of temperatures and pressures making it a good source mechanism to use for reduction. The reduction was carried out for n-hexane/air ignition studies and has been verified with the *CaltechMech* full mechanism for 500 < T < 1500 K and 0.2 < P < 5 bar. The automatic method proposed by Davidenko et al. [31] to reduce reaction mechanisms under autoignition conditions was employed. Briefly, the procedure consists in removing one reaction at a time from the detailed model and evaluating its impact on the adiabatic constant-pressure (CP) auto-ignition process. After each CP simulation, several quantities are verified, including the time to peak or the maximum heat release rate, defined as

$$\dot{q}_{max} = -\sum_{i=1}^{N} h_i \dot{\Omega}_i, \tag{9}$$

the equilibrium temperature and mean molar mass, as well as the profiles of heat release, temperature, and mean molar mass. For each quantity, the deviation induced by the reaction removal must be below a specific threshold, as defined in Table 1 of [31], for the reaction to be considered as “unimportant”. Otherwise, the reaction is classified as “important”. After all the reactions have been evaluated, the reaction inducing the lowest variation is removed from the mechanism. The procedure is repeated until only important reactions remain. The resultant reduced mechanism consists of 54 species and 265 reactions.

Figure 1 (top) plots the ignition delay times against the inverse of tem-

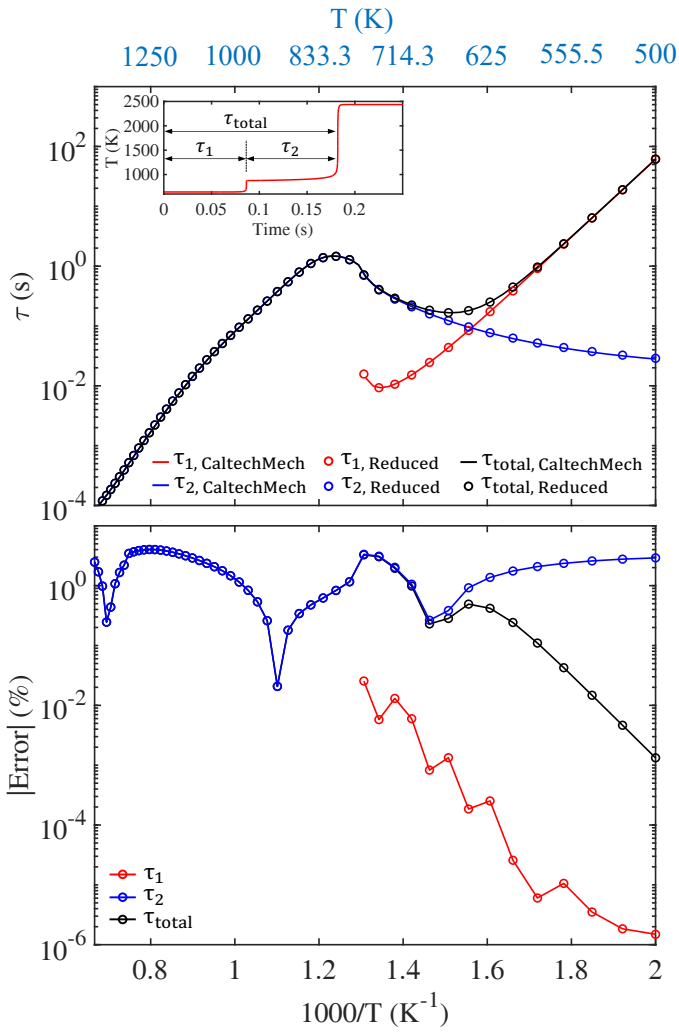

Figure 1: (Top) Ignition delay time vs. the inverse of temperature for stoichiometric nC_6H_{14}/air oxidation at 1 bar. Delay times for the first stage, τ_1, the second stage, τ_2, and the total delay, τ_{total}, for both *CaltechMech* and the reduced mechanism are shown. (Bottom) The absolute error in % of the ignition delay times computed from the reduced mechanism compared to *CaltechMech*

perature computed from zero-dimensional adiabatic constant pressure simulations at 1 bar for for stoichiometric nC_6H_{14}/air (C_6H_{14} + 9.5 (O_2 + 3.76 N_2)) in Cantera [32]. The first stage delay, τ_1, the second stage delay, τ_2,

and total delay, τ_{total} as defined in the figure for both the *CaltechMech* full mechanism and reduced mechanism are shown. In general, as the initial temperature is increased, τ_{total} decreases due to the exponential dependence of the reaction rate constant on temperature. However, the characteristic NTC region associated with a shift in dominant reaction pathways can be seen between 650 K and 800 K where an increase in τ_{total} with temperature is observed. For a given delay time, $\tau_{\text{total}} = 0.4$ s, three distinct situations can exist depending on the initial temperature. At $T_i = 600$ K, τ_1 is much longer than τ_2. At this temperature, the low-temperature chemistry is much slower than the mid- and high-temperature chemistry. Therefore, most of τ_{total} is effected by τ_1. At $T_i = 745$ K, τ_1 becomes much shorter than τ_2 as the important reactions shift. Finally, at $T_i = 908$ K, the two-stage behavior disappears entirely and ignition occurs over a single event. This behavior as the initial temperature is increased is captured by the reduced mechanism, which can be further seen in Figure 1 (bottom). The absolute error of τ_1, τ_2, and τ_{total} is shown for the zero-dimensional simulations shown in Figure 1 (bottom). The mean error of the reduced mechanism from the *CaltechMech* mechanism for τ_1, τ_2, and τ_{total} is 0.0038%, 1.96%, and 1.65%, respectively and the maximum error was 0.026%, 4.02%, and 4.02%.

This reduced mechanism was then implemented for a simulated ASTM-E659 test for gaseous nC_6H_{14}. Extensive validation was conducted, but experimental data at the conditions of interest for AIT studies (T $\sim$ 500 K, P = 1 bar) are sparse. While the measured ignition delay in the NTC region for heavy hydrocarbon fuels is well reproduced by the mechanism, there is uncertainty in the accuracy for the lower temperature and pressure conditions of AIT testing.

Surface reactions are also important to consider when discussing autoignition as they can significantly affect the reaction progress and composition near hot surfaces, influencing the overall progress of the ignition event by transport from the walls into the volume. Even Setchkin [33] in his original development of a standardized autoignition test discussed the possibly of a catalytic influence, highlighting work by numerous studies. Callendar [34] was interested in whether thermocouples had an effect on autoignition. He tested the possible catalytic effect of various metals in a test tube and found that only platinum black had any effect on ignition. Subsequent work by Thompson [35] and Matson and Dufour [36] used different metals for the construction of the walls of a reaction chamber. Variation in the autoignition temperature with wall material was found, but the effects were

attributed to changes in heat loss rather than to catalytic effects. Work by Smyth and Bryner [37] studied thermal ignition of 19 hydrocarbon fuels of varying carbon number on 3 different heated surface materials at high temperatures (>1000 K). They found a moderate effect on the critical ignition surface temperature with stainless steel having the lowest value while nickel and titanium had a larger catalytic effect. Larger hydrocarbons and higher equivalence ratios decreased the ignition temperature.

Studies on the catalytic effects of borosilicate glass or quartz on autoignition are quite sparse. Pfefferle et al. [38, 39], Griffin et al. [40] studied the catalytic effect of platinum and quartz surfaces on boundary layers flows of ethane/air mixtures at temperatures greater than 1000 K using laser-induced florescence (LIF) to observe O and OH concentrations near the heated wall. The quartz surface was found to have minimal catalytic effects whereas the platinum surface had a more important influence on ignition. A more recent study by Johnson and Mashuga [41] compared the autoignition of various hydrocarbons including nC_6H_{14} in an ASTM-E659 apparatus using a borosilicate glass and quartz flask. The AITs determined for each fuel were found to be nearly independent on the glassware type used, with variation well within the margin of error of the measurement.

Based on the sparse evidence of previous work, it is believed that the borosilicate glass used in the ASTM-E659 standard does not significantly influence the AIT for a given fuel. Therefore, surface reactions were not considered in this study. However, development and inclusion of a reliable surface reaction mechanism should be included in future work to validate this claim.

2.4. Initial and boundary conditions

Figure 2 shows the temperature boundary condition on the flask and holder as a function of height. A piece-wise linear profile in height y was imposed on the surface of the flask and was assumed constant in the holder section due to the large ceramic mass being held inside the furnace. These temperatures correspond to experimentally measured flask surface temperatures $T_1 = 521$ K, $T_2 = 527$ K, and $T_3 = 518$ K. A no-slip condition was imposed on the walls.

A 300 K sphere of gaseous nC_6H_{14} of radius $r = 1.5$ cm ($V_{liquid} \approx 86.5\mu$L) was initiated near the bottom of the flask into a fully developed unsteady flow field for pure dry air, illustrated in Figure 3. The vaporization process that occurs immediately after injection in an experiment is believed to enhance

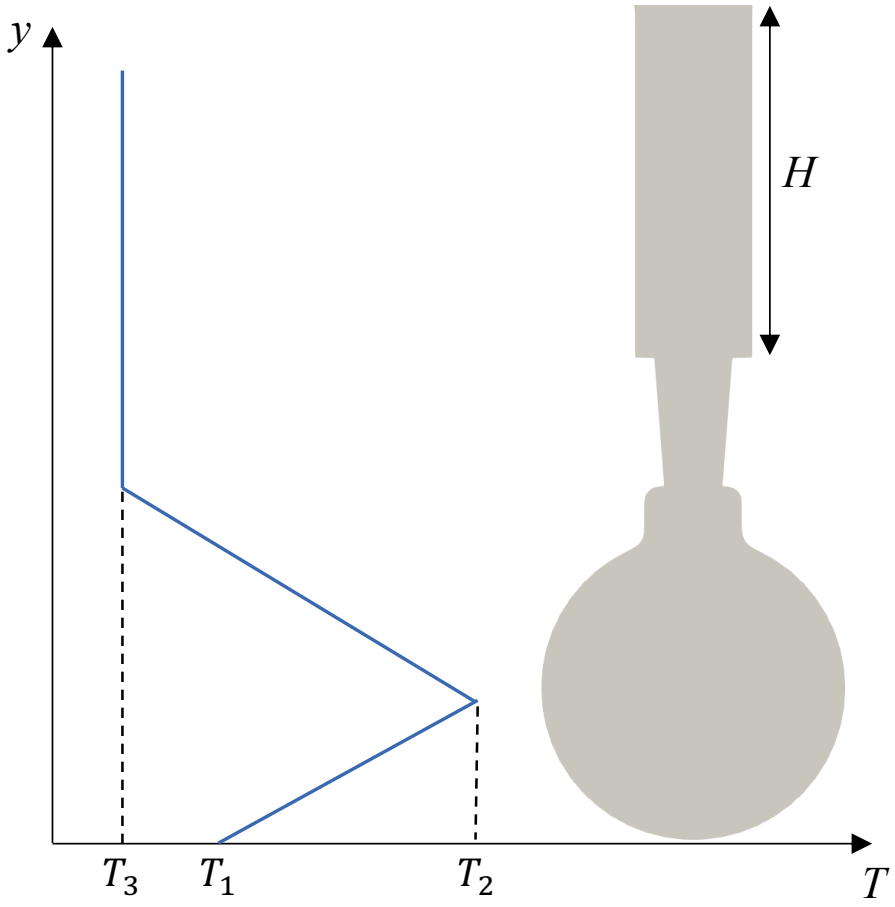

Figure 2: Height-varying temperature boundary condition

the initial mixing transient. However, it is not considered in this study. The background flow field is further discussed in Davis et al. [20].

3. Results and discussion

3.1. Verification

Grid convergence is an essential part of any numerical simulation. Standard techniques such as achieving stationary statistics for unsteady flows cannot be used since thermal ignition is a single event (i.e., they are not fully

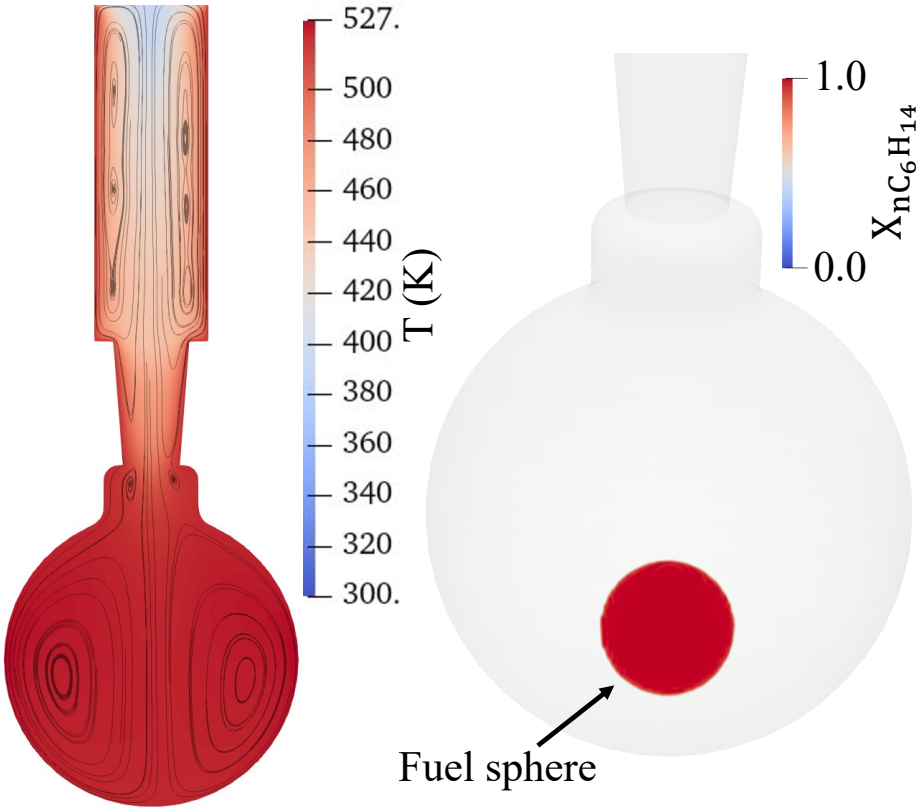

Figure 3: Vertical cross-section of the background temperature field and surface streamlines (left) and nC_6H14 fuel sphere initialization (right)

developed flow problems). Instead, other metrics specific to thermal ignition have been used to assess grid convergence including the time to ignition, τ, the maximum temperature of the first ignition stage, T_{CF}, and the vertical location of the ignition event inside the flask, y_{ign}.

Figure 4 shows the maximum temperature in the domain over time, T_{max}, along with τ, T_{CF}, and y_{ign} for three grids of varying fineness. Coarse, medium, and fine correspond to hexahedral cell sizes of 2400 μm, 1200 μm, and 600 μm, respectively. The difference between the medium and fine grids were 0.23% for τ, 0.12% for T_{CF}, and 1.52% for y_{ign}. While all three grids are relatively coarse in the context of typical flame propagation problems, the results indicate convergence of around 1% difference for grids at 600 μm

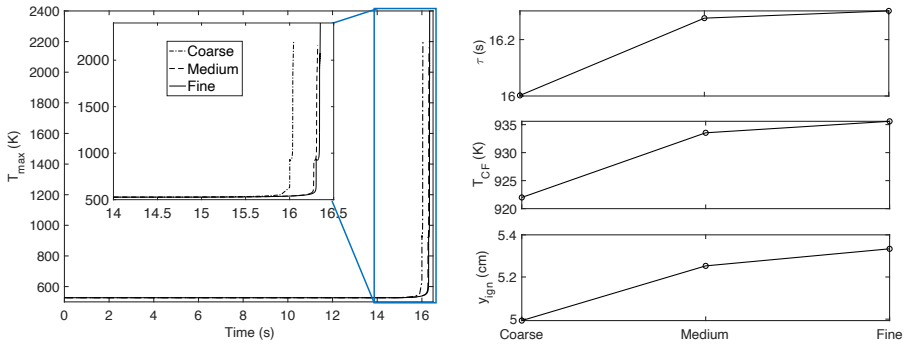

Figure 4: Maximum temperature vs. time (left) and delay time, τ, cool flame temperature. T_{CF}, and vertical ignition location, y_{ign} (right) for the three grid resolutions tested

for ignition behavior. This is possible because of the thick thermal layers ($\sim$5 cm) characteristic in autoignition testing along with the exceedingly low temperature range (500 K). While the resultant flame propagation was not the focus of our study as quantitative analysis would require substantially finer grids ($<$100 μm), preliminary verification and qualitative insights are provided in Section 3.6.

3.2. Cooking phase

After the nC_6H_{14} sphere is initialized in the flask, the cooking phase begins. It lasts for about 16 s, and is characterized by a slow progress of the chemical reaction, without a rapid change in temperature or species concentration. Figure 5 plots the nC_6H_{14} volume field in the flask at 4 instances in time through the cooking phase. Driven by gravity, the fuel initially sinks to the bottom of the flask. The fuel dispersion is mostly axisymmetric as seen by the volume field at 0.1 s, but with small asymmetry caused by the unsteady flow field induced by the open top. Both Rayleigh-Taylor and Kelvin-Helmholtz instabilities emerge due to density differences between the downward moving cold air and upward movement of heated air. We calculate a Rayleigh number using the height of the flask and holder assembly as $Ra = 7.2 \cdot 10^7$. Comparison with Rayleigh numbers reported in literature for the transition to unsteady flow ($Ra > 10^7$ [50], $10^7 < Ra < 10^8$ [51], $Ra > 10^8$ [52]), indicates that a three-dimensional unsteady flow will occur. The effect of this feature on the ignition event will be discussed later. Between 5 and 10 s, a stable, stratified concentration of nC_6H_{14} can be seen

that slowly diffuses upwards towards the top of the flask. Details regarding the nonreactive unsteady flow field and mixing of n-hexane are given in our previous study [20].

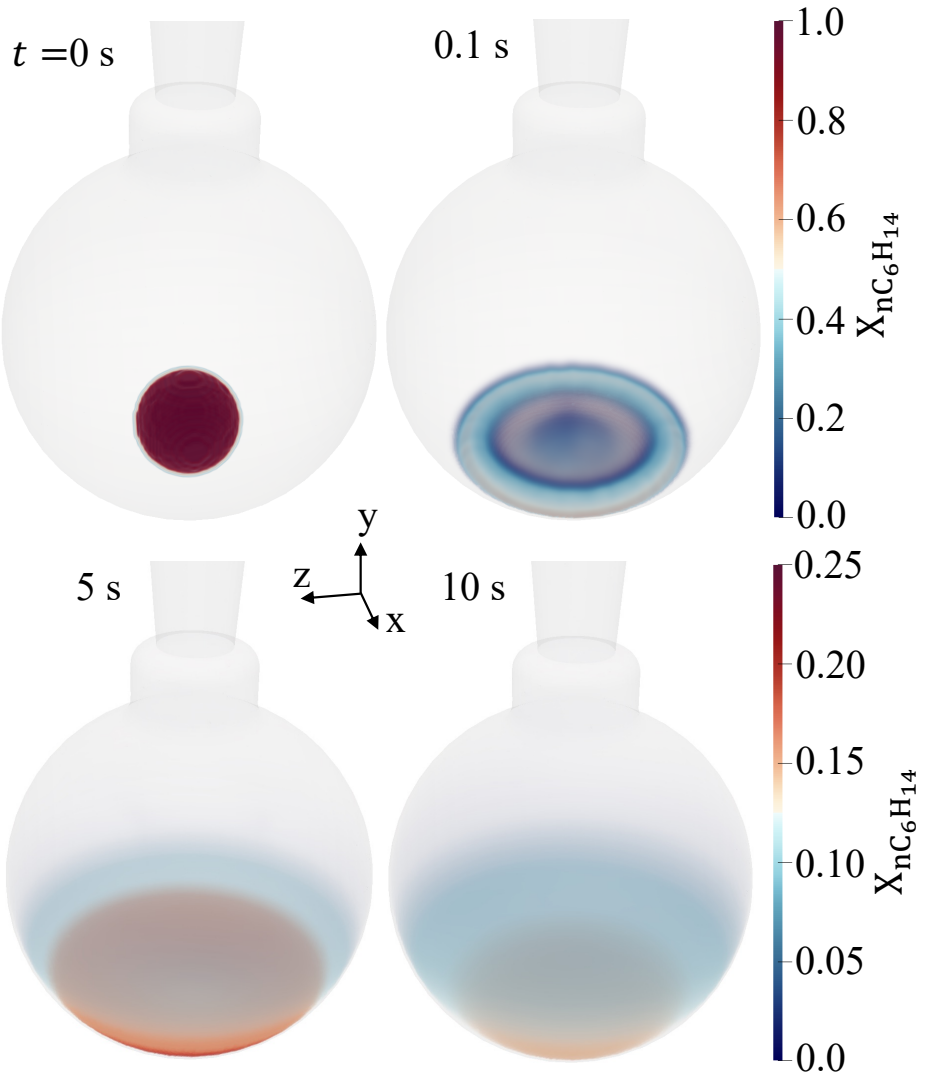

Figure 5: nC_6H_{14} volume field inside the flask during the cooking phase (0-10 s)

Figure 6 plots the volume fields of the heat release, Q, as well as the mole

fraction of three important intermediate products ($OC_6H_{11}OOH$, C_2H_4, and H_2O_2) at 10 s. For all quantities, a ring structure can be seen around the stable, nC_6H_{14}/air interface with most significant heat release and production of intermediates occurring near the walls. This is caused by the temperature distribution inside the flask. Gas temperatures near the walls can be 7 K higher than gas near the center of the flask [20]. Thus, reaction progress occurs more quickly in these regions. Over time, this ring structure moves upwards in the flask as the bulk fuel diffuses upwards until the time of ignition. The slight lopsidedness of the ring can be attributed to the asymmetry in the initial mixing transient driven by the unsteady flow generated by the open top of the flask, the resultant variation in temperature within the gas, and the sloshing behavior of the fuel as it initially sinks to the bottom of the flask.

3.3. Ignition dynamics

As time progresses past 10 s, signs of a coupled chemical-thermal runaway process can be observed. Figure 7 shows the temperature volume field and instantaneous streamlines inside the flask during the ignition event. Only temperatures above the wall temperature are colored to emphasize the characteristics of thermal ignition. As early as 14.775 s, local gas temperatures surpass the wall temperature. This time instance is omitted from the visualization as it would be a single pixel, but is important to distinguish as it marks the onset of the ignition kernel. At 15.9 s, a ring kernel can be seen near the walls around the vertical midpoint of the flask where exothermic chemical reaction causes the gas temperature to exceed the wall temperature by up to 100 K prior to ignition. The ring retains its lopsided structure originating from the initial fuel mixing transient and influences the location of the localized ignition event. The toroidal vortex flow pattern seen in Davis et al. [20] can be observed, driven by downward movement of cold air through the center of the open neck and upward movement near the walls as the gas heats up through conduction, convection, and chemical reaction. Progressing to 16.3316 seconds, the ring kernel has grown in size as the initial stages of the runaway process develop. The first stage of the ignition event can be seen propagating from a localized section of the flask with a peak temperature of 935 K. The resultant cool flame moves outwards, favoring propagation azimuthally through the ring kernel as the local temperatures are higher than near the center of the flask. The streamlines propagate out the top of the flask indicating gas expansion caused by the modest temperature rise of the

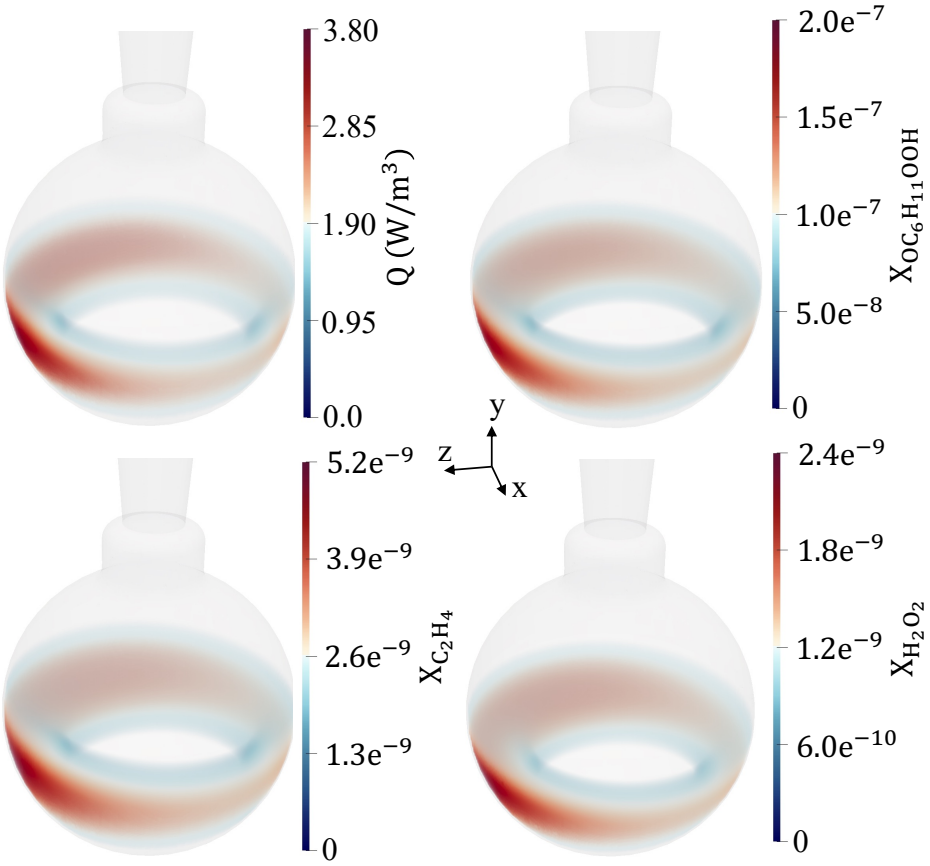

Figure 6: Q, $OC_6H_{11}OOH$, C_2H_4, and H_2O_2 volume fields inside the flask at 10 s

first stage ignition event. Around 16 ms later, at 16.3476 s, the second and final stage of ignition can be seen with a rapid and substantial increase in temperature to 2000 K. The significant increase in temperature leads to substantial gas expansion, where the speed of reactants being pushed up out the neck of the flask reach 14 m/s through the smallest cross-sectional area portion.

The two stage ignition event can also be shown graphically in Figure 8 which plots the horizontal temperature profiles through the ignition event and the center of the flask for the two stages. From Figure 8 (left), the formation of the ring kernel is seen. For early times (t = 0.1 s) after the fuel sphere

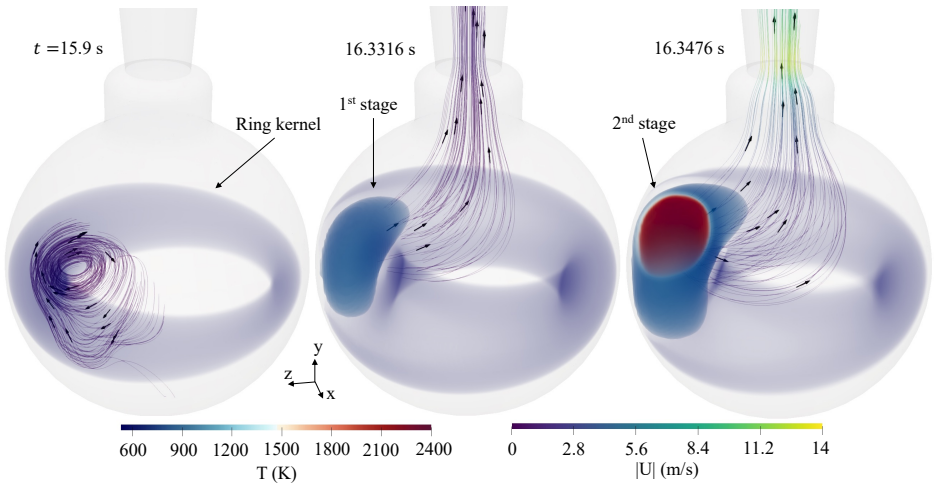

Figure 7: 3D ignition kernel evolution inside the flask. Temperatures above the wall temperature are colored as well as instantaneous streamlines near the ignition event

initialization, there is an asymmetric disturbance to the temperature field. This is caused by the asymmetric mixing immediately after the nC_6H_{14} sphere is initialized in the domain that occurs because of the unsteady flow field induced by the open top. At 10 s, after the initial transient has dampened, the hottest point remains at the wall, and a smoother temperature profile is seen with the toroidal vortex bringing colder air down through the center. Note there remains a slight asymmetry in this profile caused by small differences in reaction progress brought about by the initial transient. This difference grows as time continues and the reaction progresses and the gas temperature rises local to the location of maximum heat release. At 16.3025 s, the kernel has a peak temperature ∼60 K above the wall temperature. The opposing side of the flask has peak temperature that is only 10 K above the wall temperature at the time of the first stage of heat release, which can be observed from Figure 8 (right) between 16.3025 s and 16.3105 s and is characterized by a rapid increase in temperature to 935 K. The temperature profile at 16.3025 s is repeated to illustrate the range of temperatures that exist between the ring kernel formation and runaway process that evolves into a propagating cool flame. The cool flame propagates outwards and a localized second stage kernel forms between the wall and the cool flame front. The second stage kernel ignites approximately 40 ms after the first stage, and is associated

with a rapid increase in temperature to 2000 K and the subsequent second stage flame front chases and catches the first stage flame front.

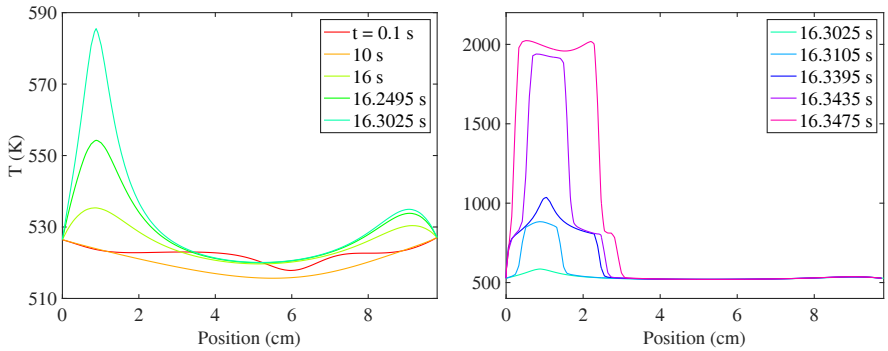

Figure 8: Temperature profiles along a horizontal line passing through the ignition event and the vertical center line of the flask for different instances in time for the 1st stage (left) and 2nd stage (right) ignition event

3.4. Experimental validation

The resultant three-dimensional reacting flow solution can be compared with an equivalent experiment in our ASTM-E659 apparatus. Figure 9 shows the results from an E659 experiment where 80 μL of liquid nC_6H_{14} is injected into a flask with a surface temperature, $T_2 = 527$ K, in accordance with the standard. These conditions were set to replicate what was simulated with gaseous nC_6H_{14}. Temperature traces are shown from three 36 AWG K-type thermocouples mounted in the center of the flask and near the walls at the same height 180° apart from each other (i.e., all three thermocouples are mounted on a horizontal line about the center of the flask). For more information on the experimental procedure and thermocouple setup, see the Supplementary Material, Davis et al. [20], and Fouchier and Shepherd [9].

After injection, a dip in the temperature can be seen across the thermocouples, strongest on $TC_{offset,2}$ indicating an asymmetric injection, vaporization, and initial mixing transient, qualitatively similar to what was observed in the simulation presented in Figures 5 and 6. The ignition delay time τ_{delay} can be measured from the time of injection to the first instance of a sharp temperature rise, $\tau_{delay} \approx 17.7$ s, longer than the ignition delay observed in the simulation ($\tau_{ign} = 16.35$ s). The increase in temperature seen by the

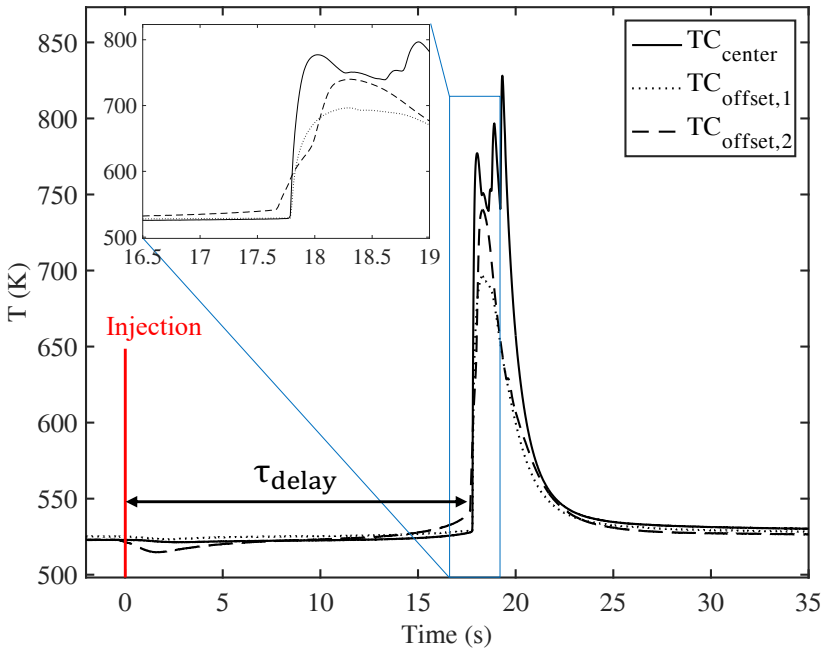

Figure 9: ASTM-E659 experiment with injection of 80 μL nC_6H_{14}. The three curves are from three 36 AWG K-type thermocouples mounted in the center of the flask and near the walls at the same height 180° apart from each other

thermocouples to 700-800 K indicates thermal ignition and flame propagation inside the flask. True flame temperatures ($\sim$ 2000 K) could not be obtained because of the 1 s response time of the thermocouples. The temperature recorded by $TC_{offset,2}$ prior to ignition in the cooking phase is larger and sees a sharp temperature rise 150 ms before $TC_{offset,1}$ and TC_{center}. This is further evidence of an ignition kernel forming near the walls and an off-center coupled chemical-thermal runaway event, as seen in the numerical simulation.

The small discrepancy in ignition delay time may be a consequence of omitting the liquid-phase and two-phase jet dynamics in the simulation. In the experiment, the injected liquid undergoes complex processes including surface impingement of the two-phase jet, spreading, and vaporization, all of which introduce a finite delay before a flammable vapor-air mixture is established. These effects, which depend on droplet breakup, heat transfer, and fuel-wall interactions, are not included in the present simulation, which assumes an initially gaseous fuel distribution. Other sources of uncertainty

include the limited validation of the reaction mechanism at AIT thermodynamic conditions. Most importantly, experimental observations by Fouchier and Shepherd [9] indicate that test-to-test variability in ignition delay times is observed even under carefully controlled testing conditions. The discrepancy for this single comparison is smaller than the observed variability, indicating that further experimental studies with statistical quantification of the uncertainty are required before further interpretation of the discrepancy.

Nevertheless, the agreement between the measured and simulated ignition delays is remarkable, indicating that the dominant ignition physics governed by fluid motion, mixing, and chemical kinetics in the gaseous phase are well represented even in the absence of detailed liquid modeling. Prior studies have shown that liquid-fueled ignition systems can be sensitive to vaporization transients [53, 54], and incorporating these effects could further improve quantitative accuracy in future work.

3.5. Lagrangian particle tracking

Particle tracking of the fluid parcel that first ignites can provide insight into the important chemical pathways that lead to thermal ignition. Since the exact ignition location is not known a priori, particle tracking must be done after the ignition event has occurred. A massless particle was injected at the time and location of ignition during post-processing. The three-dimensional numerical solution can then be integrated backwards in time to extract the approximate trajectory of the ignition particle over the entire duration of the simulation. To minimize error in this approximate trajectory, the entire solution field was sampled at 10 kHz. The trajectory of the ignition particle is shown in Figure 10 from the point of fuel initialization up to the time of ignition. The particle convects 5.6 cm upwards along the side of the flask as it heats up, following the toroidal vortex flow pattern discussed in [20].

Figure 11 (left) plots the mole fraction of nC_6H_{14} fuel along the ignition particle. During the first 15 s during the cooking phase, the nC_6H_{14} concentration increases as it mixes with the surrounding air. The unsteady downwash of cold air through the neck of the flask can be seen through the small wobbles in fuel as time evolves. At 2.2 s, the fuel concentration passes through stoichiometry. The ignition event occurs in a very rich mixture (equivalence ratio, $\phi \approx 1.8$). Figure 11 (right) zooms in on the two-stage ignition event that occurs over approximately 5 ms. The main species mole fractions are shown. Across the first stage, a rapid conversion of nC_6H_{14} and O_2 into smaller intermediate products such as ethene, C_2H_4, formaldehyde,

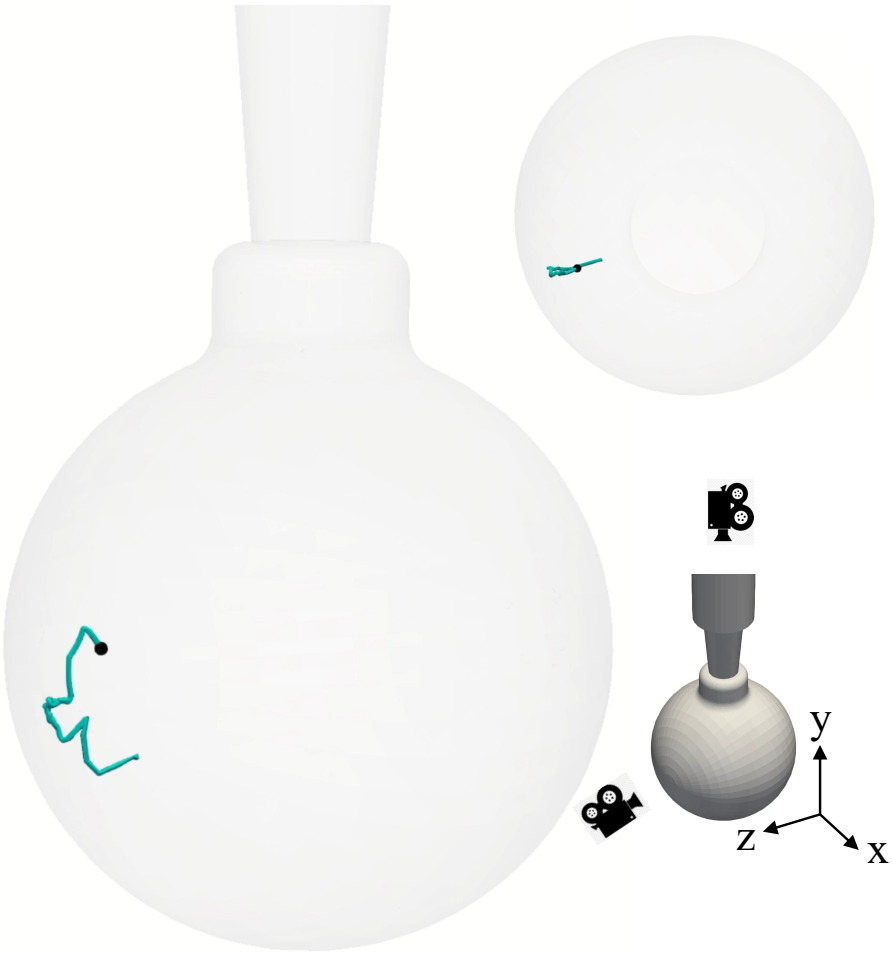

Figure 10: Ignition particle trajectory

CH_2O, and hydrogen peroxide, H_2O_2, can be seen along with a temperature increase to 935 K. At this point, the ignition progression temporarily slows down as the primary reaction pathways change. The second and final stage of ignition can then be seen with the increase in temperature to 1900 K and the conversion of remaining fuel and intermediate products into CO, CO_2, H_2O, and H_2.

The reaction pathways responsible for the two stage ignition event can be identified by looking at the heat release associated with each reaction as well as rate of production of important species along the tracked particle path.

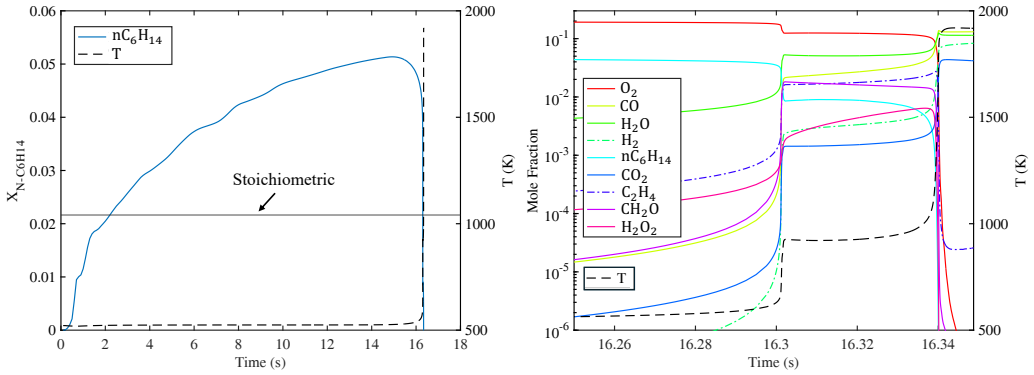

Figure 11: nC_6H_{14} mole fraction over the entire simulation time (left) and major species mole fraction during the two stage ignition event (right) along the ignition particle path. The temperature (- -) is also shown in both plots

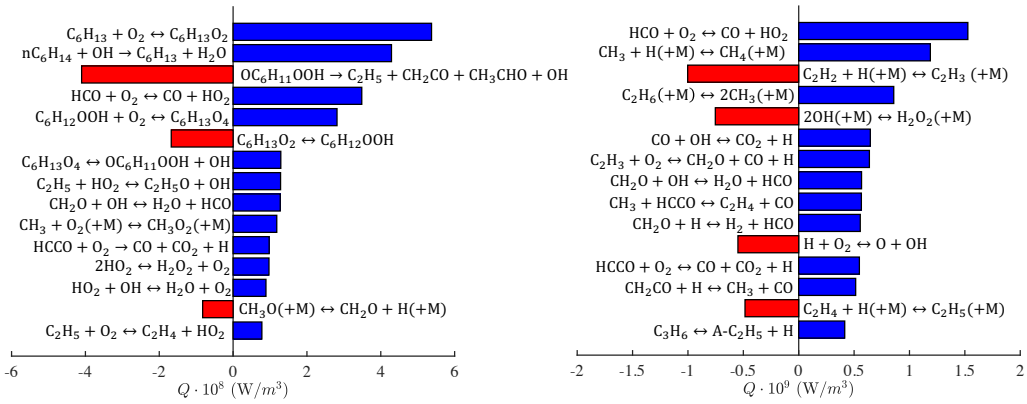

Figure 12: Total heat release of the top reactions for the first ignition stage (left) and the second ignition stage (right)

The time-integrated heat release for top reactions across each ignition stage are shown in Figure 12. The following reaction pathway associated with the first stage ignition event can be seen from Figure 12 (left):

$$nC_6H_{14} + OH \rightarrow C_6H_{13} + H_2O \qquad \text{(R1)}$$

The first step is the H-abstraction of the nC_6H_{14} fuel by an OH to produce

a hexyl radical (C_6H_{13}) and H_2O.

$$C_6H_{13} + O_2 \rightarrow C_6H_{13}O_2 \tag{R2}$$

The C_6H_{13} then gets attacked by O_2 molecules. However, instead of further H-abstraction, the O_2 attaches to the C_6H_{13} to form $C_6H_{13}O_2$. This reaction is very exothermic and is the primary reaction responsible for the first stage heat release.

$$C_6H_{13}O_2 \rightarrow C_6H_{12}OOH \tag{R3}$$

$$C_6H_{12}OOH + O_2 \rightarrow C_6H_{13}O_4 \tag{R4}$$

An isomerization reaction followed by the addition of another O_2 onto the $C_6H_{12}OOH$ molecule produces a hydroperoxyhexylperoxy radical ($C_6H_{13}O_4$). While the isomerization reaction in this step is endothermic, the addition reaction makes this sequence of two reactions exothermic.

$$C_6H_{13}O_4 \rightarrow OC_6H_{11}OOH + OH \tag{R5}$$

$$OC_6H_{11}OOH \rightarrow C_2H_5 + CH_2CO + CH_3CHO + OH \tag{R6}$$

The final sequence involves decomposition of the $OC_6H_{13}O_4$ into $OC_6H_{11}OOH$ and another OH. The $OC_6H_{11}OOH$ molecule then breaks apart into smaller ketones and aldehydes, such as ketene (CH_2CO) and acetaldehyde (CH_3CHO). Along with the ethyl radical (C_2H_5), these ketones and aldehydes branch into many pathways that produce the stable intermediates observed during the period between the two stages of heat release (i.e., CO, C_2H_4, and CH_2O). This oxidation pathway is overall an exothermic sequence. Note that two OH molecules are produced from a single OH molecule that initiates the overall reaction. Thus, this sequence leads to the multiplicative production of OH molecules that ultimately drive the first stage coupled chemical-thermal runaway. The first stage ignition event described by reactions (R1)-(R6) seen in the autoignition simulation is consistent with what has been discussed for nC_6H_{14} oxidation by Mével et al. [42] and more broadly for other heavy hydrocarbon fuels [29, 43].

The second stage is evident from Figure 11 (right) as a rapid temperature rise to 1900 K and completion of the reaction to form CO, CO_2, H_2O, and H_2. The 1900 K ignition temperature is significantly lower than what would be expected from a stoichiometric mixture of nC_6H_{14}/air ($\sim$2400 K). This can be attributed to the high equivalence ratio of the mixture ($\phi = 1.8$)

present at the time of ignition. The temporal heat release, Q, and rate of production (ROP) traces for the top reactions along the ignition particle path can be plotted for the second stage (Figure 13) which can broken up into two temperature ranges: 1.) 900 K $<$ T $<$ 1450 K and 2.) T $>$ 1450 K.

We first examine the 900 K $<$ T $<$ 1450 K range. Looking at Figure 12 (right), the oxidation reaction HCO + O_2 $\rightarrow$ CO + HO_2 releases the most heat during the second stage. From the temporal heat release for the top reactions shown in Figure 13a, this reaction occurs early on while the temperature is below 1450 K. The reaction is sustained by the generation of formyl radicals (HCO) by the large amount of CH_2O produced during the first stage. This occurs primarily from the reactions CH_2O + H $\rightarrow$ H_2 + HCO and CH_2O + OH $\rightarrow$ H_2O + HCO as can be seen from the top reactions for the rate of production of HCO in Figure 13c. This reaction continues to release a significant amount of heat until around 1450 K. As the temperature continues to increase beyond 1450 K, the HCO molecules preferentially decompose into H and CO instead of reacting with the O_2. Reaction pathways involving CH_3 and OH become the dominant exothermic processes to drive the temperature increase.

The temperature range, T $>$ 1450 K, can be identified by an even sharper temperature rise associated with a shift in dominant reaction pathways from those involving HCO to those involving CH_3 and OH precursors. The traditional mechanism for coupled chemical-thermal runaway of heavy alkanes by an OH carrier [29] can be seen from the second stage heat release and rate of production of OH shown in Figure 12 (right) and Figure 13b. The prominent chain branching reactions H_2O_2 (+M) $\rightarrow$ 2OH (+M) and H + O_2 $\rightarrow$ O + OH are followed by the exothermic chain terminating recombination reaction CO + OH $\rightarrow$ CO_2 + H. However, because the ignition event occurs in a very rich mixture, there is a lack of oxygen to drive the conversion from CO $\rightarrow$ CO_2. As a result, this process does not release as much heat during the second stage ignition process as would be expected from a stoichiometric analysis.

Instead, reaction pathways involving methyl, CH_3, provide the most significant contribution to the heat release above 1450 K. This can be seen in Figure 12 (right) and Figure 13d. The addition of an H atom onto CH_3 to produce CH_4 as well as the recombination of two CH_3 molecules into ethane, C_2H_6, release substantial heat. These exothermic CH_3 reactions are sustained by the conversion of C_2H_4 formed during the first stage ignition event into CH_3 through aldehydes and ketones, C_2H_4 $\rightarrow$ CH_2CHO $\rightarrow$ CH_2CO $\rightarrow$

CH_3, as well as the reverse reaction $CH_4 + H \rightarrow CH_3 + H_2$ that produces H_2 as a byproduct.

The lack of oxygen present during the ignition event in a fuel rich region shifts the prominent reaction pathways critical for the second stage coupled chemical-thermal runaway. As a result, HCO and CH_3 reaction pathways become more significant. This leads to a decrease in ignition temperature and the larger amounts of CO and H_2 compared to CO_2 in the combustion products.

3.6. Flame propagation

While thermal ignition was the primary focus of this study, the subsequent flame propagation can provide further insights into the autoignition process and aid in developing more stringent testing standards.

3.6.1. Preliminary verification

The resultant flame propagation through the flask and holder section after the two-stage ignition event must be scrutinized, especially since the 600 μm grid size is quite coarse when discussing flames. However with limited optical access, experimental validation of the flame speed is challenging. Comparisons to the expected flame speed from well-resolved one-dimensional freely propagating laminar flame calculations provide an obtainable metric for preliminary verification. To this extent, one-dimensional flames were simulated in Cantera [32]. More information about the modeling can be found in the Supplementary Material. Careful consideration of a number of factors must be made when comparing flame speeds between the three-dimensional autoignition simulation and a simplified one-dimensional laminar flame. The following two observations are made:

- At the time of ignition, the reactants are stratified throughout the flask which produces flame propagation through a vertically stratified mixture after ignition whereas the one-dimensional laminar flame calculations consider a homogeneous mixture.

- Two stage coupled chemical-thermal runaway in the autoignition simulation produces a transient two stage flame propagation for early times after ignition. This will not be captured by the steady one-dimensional laminar flame model

To best address these issues, a point in time and space is taken inside the flask where the flame propagation is horizontal and enough time has passed such that the second stage flame front has overtaken the first stage flame front. Because the injected nC_6H_{14} is mostly stratified after the initial mixing transient and prior to ignition as shown in Figure 5 and discussed in Davis et al. [20], locations of the flame that propagate horizontally are approximately homogeneous. Ensuring enough time has passed allows a single flame front to propagate into a reactant mixture that has not undergone significant chemical reaction. This can be easily initialized into the one-dimensional flame model. One possible horizontal line that satisfies these requirements is shown in Figure 14 at a height of y = 6.25 cm and at t = 16.35065 s where the local equivalence ratio is lean, $\phi \approx 0.80$. The velocity can then be projected onto and plotted along this axis. Figure 15 plots the projected velocity, U_{proj}, and the temperature along the chosen horizontal line. The flame speed can then be calculated as the velocity difference across the flame front as $\Delta u \approx 2.59$ m/s.

The estimated flame speed can easily be obtained from the 1D freely-propagating flame model through a mass balance as

$$u_f = u_b - S_L = \big(\frac{\rho_u}{\rho_b} - 1\big) S_L \,, \tag{10}$$

where u_f is the estimated flame speed, u_b and ρ_b are the burnt gas speed and density, respectively, ρ_u is the unburnt gas density, and S_L is the laminar burning velocity. Estimating the unburnt conditions from the 3D autoignition simulation ($T_u \approx 522$ K and equivalence ratio, $\phi \approx 0.80$), the following densities and laminar burning velocity are calculated:

- $\rho_u \approx 0.6966$ kg/m^3
- $\rho_b \approx 0.1665$ kg/m^3
- $S_L \approx 0.828$ m/s

Substituting these values into Eq. (10), the flame speed can be estimated as $u_f = 2.66$ m/s (2.7% difference to the 3D simulation flame speed).

The laminar flame thickness can also be estimated using the maximum temperature gradient across the flame according to [44] as:

$$\ell_f = \frac{T_b - T_u}{\big(dT/dx\big)_{max}} \,, \tag{11}$$

where T_b is the burnt gas temperature and T_u is the unburnt gas temperature. For more information, see the Supplementary Material. From the 1D freely-propagating flame model, $\ell_f \approx 300\mu$m. From Figure 15, the flame thickness calculated in 3D autoignition simulation is an order of magnitude larger at $\sim$3.3 mm. This is most likely because the grid size of 600 μm is too large to adequately simulate the flame propagation after the ignition event and numerical diffusion artificially thickens the flame front. However, numerous studies of various fuel/oxidizer mixture flame thicknesses suggest that ℓ_f underestimates the actual flame thickness from experiments and numerical simulation. Bradley et al. [45] suggest the true flame thickness measured by single shot OH planar laser-induced florescence (PLIF) of spherical explosions of iso-octane flames is larger than ℓ_f by a factor of 30. Other studies for methane/air flames suggest that the true flame thickness is between 3 and 50 times larger than ℓ_f [46, 47]. While sparse data exists, if this is also the case for nC_6H_{14} flames, the estimated flame thickness and propagation from the presented simulation may be properly resolved.

Despite the coarse grid and expected numerical diffusion, the 3D autoignition simulation adequately reproduces the expected flame speed from the highly resolved 1D freely-propagating flame model. While a finer grid, likely < 100 μm, is necessary to quantitatively analyze the flame propagation after the ignition event, the solution is deemed sufficient to qualitatively assess flame development and behavior as time evolves.

3.6.2. Flame propagation

Figure 16 plots the temperature and colorbar-saturated nC_6H_{14} mass fraction as well as CO_2 and H_2 mass fraction fields on a vertical slice through the flask and holder at various times after the ignition event. The nC_6H_{14} mass fraction field is intentionally saturated to show the movement of fuel out of the flask. This occurs in a very lean concentration and is most easily visible using a saturated colorbar. At early times in Figure 16a and 16b, the flame is ignited near the wall through a localized two-stage ignition event that was thoroughly analyzed in Section 3.1 - 3.5. As early as 16.3488 s, the nC_6H_{14} fuel can be seen being ejected from the flask as a jet through the neck as the gas rapidly expands from the ignition event. At 16.3533 s, the flame has expanded radially through the flask. Because the fuel is stratified at the time of ignition (see Figure 5), the nC_6H_{14} concentration at the bottom of the flask is very rich and above the upper flammability limit (7.5% by volume, [48]). Thus, the flame cannot propagate into this region. Instead,

the flame is convected up out of the neck of the flask, rapidly accelerating and stretching into a thin front through one side of the constriction near the ignition event. The inability of the flame to propagate across the entire width of the neck is likely caused by the strong sheer created by the velocity gradients in the constriction due to the expelling of gas through the flask top. A similar effect was observed by Iida et al. [49] for premixed flame propagation into a narrow channel. The propagation of the flame out of the flask is only possible because of the ejected unburnt fuel caused by the ignition event itself. Later in time, at 16.35344 s, the flame can be seen expanding into the holder section above the flask and becoming unsteady. This is a consequence of the highly unsteady flow that already exists in this region of the apparatus [20]. Progressing to 16.35595 s and later, 16.3585 s, the flame front can be seen breaking apart into numerous smaller flamelets that are convected upwards and eventually out of the flask in what has been observed and identified in experiments as "Mode I" ignition with a visible flame [8]. This breakup of the flame can be attributed to numerous factors including unsteady mixing mixing, heat loss to the cooler surrounding gas, stretching of the flame surface caused by differential velocities, and localized regions of very lean fuel concentrations below the lower flammability limit. This transition is consistent with known flame-flow interactions, where curvature and strain can wrinkle or fragment the flame surface [55, 56, 57].

The differences in reaction pathways discussed in Section 3.5 as a result of the fuel stratification in the flask at the time of ignition can also be seen from Figures 16a, 16c, and 16d. After the ignition event in a fuel-rich region ($\phi \approx 1.8$), the flame front that got convected upwards reaches a maximum temperature around 2400 K where the fuel concentration is close to stoichiometry near the top of the flask. This rapid temperature rise coincides with a peak in the exothermic chain terminating recombination reaction CO + OH $\rightarrow$ CO_2 + H (further shown in Figure 13b) which dominates the conversion of CO into CO_2 and confirms that it is the dominant contributor to heat release in this region. Although the peak temperature decreases to around 1800 K, this pathway remains the dominant mechanism for heat release as the flame propagates into a lean mixture ($\phi < 1$) up through the neck of the flask and into the holder.

The downward propagating flame front occurs in a rich mixture ($\phi > 1.8$). The lower peak temperature of around 1600 K and significantly higher concentration of H_2 up to 9% mole fraction (compared with $\approx$ 1% mole fraction in the stoichiometric and fuel lean regions) in the products shown in

Figure 16 is a result of an alternative dominant reaction pathway involving CH_3 as further discussed in Section 3.5. This flame front moves only 2 cm downwards from the ignition location before being quenched as it reaches a very rich fuel/air mixture ($\phi >> 1.8$).

4. ASTM-E659 Testing Insights

The numerical autoignition simulation of nC_6H_{14} presented in this paper provide a first insight to the ignition process during an ASTM-E659 test.

The nonuniform temperature distribution within the flask brought about by small surface temperature differences inevitable in experiments and intrusion of cold gas through the open top through the center of the flask prescribed by the ASTM-E659 standard [20, 6] leads to enhanced chemical reaction in a localized ring near the wall where the temperature is largest. In addition, the instantaneous temperature and velocity field inside the flask at the time of fuel injection drives a slightly asymmetric initial mixing transient that leads to a localized off-center ignition event. The highly unsteady fuel vaporization process not modeled in this work most likely also contributes to this phenomenon as well as additional variability in results [9]. This highlights the sensitivity of the ignition behavior to the fuel injection technique and care should be taken to reduce the variability in results.

For short duration tests with heavy fuels (typically < 100 s as discussed by Davis et al. [20]), as shown for nC_6H_{14} in this study, ignition occurs in a vertically stratified layer of fuel. The degree of stratification will depend on the amount of fuel injected as well as the surface temperature that can affect the ignition delay time and can have a substantial effect on the resultant flame propagation. For longer duration tests that are several minutes long, ignition will occur in a homogeneous mixture possibly through different specific reaction pathways.

For heavy hydrocarbons, such as nC_6H_{14}, that exhibit an NTC region, a two-stage ignition behavior is most likely present for temperatures slightly larger than the AIT as shown in this study, where substantial gas expansion pushes unburnt fuel and the flame out of the flask and holder assembly as a visible flame commonly referred to as "Mode I" ignition as defined by Martin and Shepherd [8]. Preliminary simulations suggest that slightly cooler surface temperatures significantly slow down the ignition process. Under these conditions, natural convection becomes more influential, causing the heated gas to rise and shifting the ignition location toward the neck of the

flask. This upward movement, along with interactions between heat release and cooling effects from the surrounding air, appears to play a key role in the emergence of distinct ignition behaviors described by Martin and Shepherd [8].

5. Conclusions

In this study, numerical modeling of gaseous nC_6H_{14} autoignition in our laboratory's ASTM-E659 apparatus was performed for a single test case corresponding to a given wall temperature distribution and injected fuel volume/temperature. A reduced kinetic mechanism suitable for multidimensional reacting flow simulations was developed for nC_6H_{14}/air oxidation including low temperature chemistry.

It was found that after initialization of the gaseous nC_6H_{14} sphere, the fuel immediately sinks to the bottom of the flask and begins to slowly diffuse upwards. Chemical reaction begins slowly and most prominently near the walls where the local gas temperature is the hottest, forming many intermediate species including $OC_6H_{11}OOH$, C_2H_4, and H_2O_2. The formation of intermediates is nearly symmetric in the azimuthal direction around the vertical center line in the flask, but small variations arise due to asymmetry in the initial mixing transient caused by the unsteady flow generated by the open top in the flask. These small variations grow over time during the cooking phase and ultimately lead to a localized ignition event. At 15.9 s, a lopsided ring kernel is seen near the walls around the vertical midpoint of the flask in a rich fuel-air mixture ($\phi \approx 1.8$) where exothermic chemical reaction causes the gas temperature to exceed the wall temperature by up to 100 K prior to coupled chemical-thermal runaway. Ignition follows in a two-stage sequence. The first stage occurs as a rapid increase in temperature to 935 K. The second stage follows from inside the gas processed by the first stage $\sim$40 ms later with a conversion of the intermediate species into products and rapid increase in temperature to 1900 K.

Massless lagrangian particle tracking was performed on the fluid parcel that first ignites to understand the chemical pathways that occur prior to and during coupled chemical-thermal runaway. An exothermic low-temperature oxidation pathway $nC_6H_{14} \rightarrow C_6H_{13}O_2 \rightarrow C_6H_{13}O_4 \rightarrow OC_6H11OOH \rightarrow$ ketones + aldehydes was identified to be responsible for the first stage. Instead of the traditional high-temperature oxidation pathways converting $CO \rightarrow CO_2$ by OH radicals, oxidation of HCO molecules generated by the large

amounts of CH_2O produced from the first stage was found to drive coupled chemical-thermal runaway of the second stage while $T < 1450$ K. Once $T > 1450$ K, reaction pathways involving recombination of CH_3 molecules become the primary process for heat release due to the lack of O_2 molecules present at the time of ignition. This results in higher concentration of CO and H_2 in the products compared to CO_2, as typically seen for mixtures closer to stoichiometry.

Lastly, a preliminary study of the flame propagation through the flask and holder after thermal ignition revealed agreement within 2.7% of the expected flame speed calculated from highly-resolved one-dimensional freely-propagating flame calculations, even though a coarse numerical grid artificially thickened the flame. The three-dimensional flame propagation solution was deemed sufficient for qualitative analysis. After ignition, gas expansion caused by the flame propagation ejects unburnt fuel in the flask out through the top of the flask as a jet. The flame, quenched at the bottom of the flask by a exceedingly rich mixture, is convected upwards, chasing the unburnt fuel. Upon entering the constriction in the neck of the flask, the flame rapidly accelerates and stretches into a long, thin front. The lean flame eventually becomes unstable and breaks apart into numerous smaller flamelets in the holder section because of unsteady mixing, heat loss, and stretching. These flamelets continue convecting upwards through the holder and out the top in what is believed to be experimentally observed as "Mode I" ignition.

Acknowledgements

This research was carried out in the Explosion Dynamics Laboratory of the California Institute of Technology and was supported by The Boeing Company through a Strategic Research and Development Relationship Agreement CT-BA-GTA-1.

References

[1] M. Hattwig, H. Steen (Eds.), Handbook of Explosion Prevention and Protection, Wiley-VCH Verlag GmbH & Co. KGaA, Weinheim, FRG, 2004.

[2] V. Babrauskas, Ignition Handbook, Fire Sciences Publishers, Society of Fire Protection Engineers, 2003.

[3] P. Bowes, Self-heating: evaluating and controlling the hazards, Department of the Environment, Building Research Establishment (1984).

[4] U. C. Guard, Chemical hazard response information system (chris)-hazardous chemical data, Commandant Instruction 16465 (1999).

[5] S. Zakel, E. Brandes, V. Schröder, Reliable safety characteristics of flammable gases and liquids–the database chemsafe, J. Loss Prev. Process Ind. 62 (2019) 103914.

[6] ASTM-E659-24, Standard test method for autoignition temperature of liquid chemicals, American Society for Testing and Materials, 2024.

[7] ISO/IEC, ISO/IEC 80079-20-1: Explosive Atmospheres - Part 20-1: Material Characteristics for Gas and Vapor Classification-Test Methods and Data, Technical Report, International Organization for Standardization, 2017.

[8] C. D. Martin, J. E. Shepherd, Low temperature autoignition of jet a and surrogate jet fuel, J. Loss Prev. Process Ind. 71 (2021) 104454.

[9] C. Fouchier, J. Shepherd, ASTM-E659 standardized test analysis and results for synthetic paraffinic kerosene, Journal of Loss Prevention in the Process Industries 94 (2025) 105568.

[10] P. Lüth, E. Brandes, T. Stolz, Interlaboratory Test 2012 - 2013 on the Method EN 14522:2005 "Determination of the Auto Ignition Temperature of Gases and Vapours" - IEC 60079-20-1, Part 7 "Method of Test for Autoignition Temperature: Final Report, BAM, Bundesforschungsanstalt für Materialforschung und -prüfung, Berlin, 2014.

[11] C. Johnson, C. V. Mashuga, Reconsidering autoignition in the context of modern process safety: Literature review and experimental analysis, J. Loss Prev. Process Ind. 81 (2023) 104963.

[12] B. Tyler, An experimental investigation of conductive and convective heat transfer during exothermic gas phase reactions, Combust. Flame 10 (1966) 90–91.

[13] P. Ashmore, B. Tyler, T. Wesley, Experimental investigations of conductive and convective heat transfer in relation to thermal ignitions,

in: Symposium (International) on Combustion, volume 11, 1967, pp. 1133–1140.

[14] D. Jones, Convective effects in enclosed, exothery reacting gases, International Journal of Heat and Mass Transfer 17 (1974) 11–21.

[15] R. J. Kee, C. S. Landram, J. C. Miles, Natural Convection of a Heat-Generating Fluid Within Closed Vertical Cylinders and Spheres, Technical Report SAND75-8610, Sandia Laboratories, Livermore CA, 1975.

[16] M. Silakova, V. Smetanyuk, H. Pasman, Model, software for calculation of ait and its validation, 2006. URL: `https://www.morechemistry.com/SAFEKINEX/`, Deliverable No. 18 of SAFEKINEX:SAFe and Efficient hydrocarbon oxidation processes by KINetics and Explosion eXpertise.

[17] A. Campbell, S. Cardoso, A. Hayhurst, A comparison of measured temperatures with those calculated numerically and analytically for an exothermic chemical reaction inside a spherical batch reactor with natural convection, Chemical Engineering Science 62 (2007) 3068–3082.

[18] J. Melguizo-Gavilanes, P. Boettcher, R. Mével, J. Shepherd, Numerical study of the transition between slow reaction and ignition in a cylindrical vessel, Combustion and Flame 204 (2019) 116–136.

[19] B. Tyler, A. Tuck, Heat transfer to a gas from a spherical enclosure: Measurements and mechanism, International Journal of Heat and Mass Transfer 10 (1967) 251–253.

[20] B. Davis, C. Fouchier, J. Shepherd, Fluid motion and heat transfer in an ASTM-E659 apparatus, Journal of Loss Prevention in the Process Industries 94 (2025) 1055558.

[21] C. D. Martin, Experiments in Thermal Ignition: Influence of Natural Convection on Properties of Gaseous Explosions, Ph.D. thesis, California Institute of Technology, 2023.

[22] C. F. Curtiss, J. O. Hirschfelder, Transport properties of multicomponent gas mixtures, J. Chem. Phys. 17 (1949) 550–555.

[23] T. Coffee, J. Heimerl, Transport algorithms for premixed, laminar steady-state flames, Combust. Flame 43 (1981) 273–289.

[24] R. I. Issa, Solution of the implicitly discretised fluid flow equations by operator-splitting, J. Comput. Phys. 62 (1986) 40–65.

[25] G. Strang, On the construction and comparison of difference schemes, SIAM J. Numer. Anal. 5 (1968) 506–517.

[26] A. Cuoci, A. Frassoldati, T. Faravelli, E. Ranzi, A computational tool for the detailed kinetic modeling of laminar flames: Application to C_2H_4/CH_4 coflow flames, Combust. Flame 160 (2013) 870–886.

[27] A. Cuoci, A. Frassoldati, T. Faravelli, E. Ranzi, Numerical modeling of laminar flames with detailed kinetics based on the operator-splitting method, Energy & fuels 27 (2013) 7730–7753.

[28] C. K. Westbrook, F. L. Dryer, Chemical kinetic modeling of hydrocarbon combustion, Progress in energy and combustion science 10 (1984) 1–57.

[29] F. Battin-Leclerc, Detailed chemical kinetic models for the low-temperature combustion of hydrocarbons with application to gasoline and diesel fuel surrogates, Prog. Energy Combust. Sci. 34 (2008) 440–498.

[30] G. Blanquart, P. Pepiot-Desjardins, H. Pitsch, K. Narayanaswamy, CaltechMech, ???? URL: `https://www.theforce.caltech.edu/CaltechMech/`, accessed June 2018.

[31] D. Davidenko, R. Mével, G. Dupré, Numerical study of the detonation structure in rich H_2-NO_2/N_2O_4 and very lean H_2-N_2O mixtures, Shock Waves 21 (2011) 85–99.

[32] D. G. Goodwin, H. K. Moffat, I. Schoegl, R. L. Speth, B. W. Weber, Cantera: An object-oriented software toolkit for chemical kinetics, thermodynamics, and transport processes, 2021. Version 2.5.1.

[33] N. P. Setchkin, Self-ignition temperatures of combustible liquids, Journal of Research of the National Bureau of Standards 53 (1954) 49.

[34] H. Callendar, Detonation and dopes, Engineering 123 (1927) 147,182,210.

[35] N. Thompson, Autoignition of flammable liquids, Industrial Engineering Chemistry 21 (1929).

[36] A. Matson, R. Dufour, The Lower Limit of Flammability and the Autogenous Ignition Temperature of Certain Solvent Vapors Encountered in Ovens, Underwriters' Laboratories, 1950.

[37] K. C. Smyth, N. P. Bryner, Short-duration autoignition temperature measurements for hydrocarbon fuels near heated metal surfaces, Combust. Sci. Technol. 126 (1997) 225–253.

[38] L. D. Pfefferle, T. A. Griffin, M. Winter, D. R. Crosley, M. J. Dyer, The influence of catalytic activity on the ignition of boundary layer flows part i: Hydroxyl radical measurements, Combustion and flame 76 (1989, Part I) 325–338.

[39] L. D. Pfefferle, T. A. Griffin, M. J. Dyer, D. R. Crosley, The influence of catalytic activity on the gas phase ignition of boundary layer flows part ii. oxygen atom measurements, Combustion and Flame 76 (1989, Part II) 339–349.

[40] T. A. Griffin, M. Calabrese, L. D. Pfefferle, A. Sappey, R. Copeland, D. R. Crosley, The influence of catalytic activity on the ignition of boundary layer flows. part iii: Hydroxyl radical measurements in low-pressure boundary layer flows, Combustion and flame 90 (1992) 11–33.

[41] C. Johnson, C. V. Mashuga, Characterizing the autoignition behavior of simple paraffins and alcohols; comparisons and implications, J. Loss Prev. Process Ind. 77 (2022) 104773.

[42] R. Mével, F. Rostand, D. Lemarié, L. Breyton, J. Shepherd, Oxidation of n-hexane in the vicinity of the auto-ignition temperature, Fuel 236 (2019) 373–381.

[43] H. J. Curran, Developing detailed chemical kinetic mechanisms for fuel combustion, Proc. Combust. Inst. 37 (2019) 57–81.

[44] D. Spalding, V. Jain, The theory of steady laminar spherical flame propagation: Analytical solutions, Combust. Flame 5 (1961) 11–18.

[45] D. Bradley, C. Sheppart, R. Woolley, D. Greenhalgh, R. Lockett, The development and structure of flame instabilities and cellularity at low Markstein numbers in explosions, Combustion and flame 122 (2000) 195–209.

[46] D. Bradley, P. H. Gaskell, X.-J. Gu, Burning velocities, Markstein lengths, and flame quenching for spherical methane-air flames: a computational study, Combustion and flame 104 (1996) 176–198.

[47] M. A. Turner, T. T. Paschal, P. Parajuli, W. D. Kulatilaka, E. L. Petersen, Resolving flame thickness using high-speed chemiluminescence imaging of OH* and CH* in spherically expanding methane–air flames, Proc. Combust. Inst. 38 (2021) 2101–2108.

[48] National Toxicology Program, National Toxicology Program Chemical Repository Database, 1992.

[49] N. Iida, O. Kawaguchi, G. T. Sato, Premixed flame propagating into a narrow channel at a high speed, part 1: Flame behaviors in the channel, Combustion and flame 60 (1985) 245–255.

[50] G. de Vahl Davis, Natural convection of air in a square cavity: a bench mark numerical solution, International Journal for Numerical Methods in Fluids 3 (3) (1983) 249–264.

[51] S. Ostrach, Natural Convection in Enclosures, J. Heat Transfer 110 (1988) 1175–1190.

[52] A. Bejan, Convection Heat Transfer, John Wiley & Sons, Hoboken, NJ, 2013.

[53] W. A. Sirignano, Fluid Dynamics and Transport of Droplets and Sprays, Cambridge University Press, Cambridge, UK, 1999.

[54] S. R. Turns, An Introduction to Combustion: Concepts and Applications, 3rd ed., McGraw-Hill Education, New York, NY, 2012.

[55] C. K. Law, C. J. Sung, Structure, aerodynamics, and geometry of premixed flamelets, Progress in Energy and Combustion Science 26 (2000) 459–505.

[56] T. Poinsot, D. Veynante, Theoretical and Numerical Combustion, RT Edwards, Inc., 2005.

[57] S. Bane, R. Mével, J. E. Shepherd, Instability of a flame front in a lean H_2-N_2O mixture, 63rd APS Division of Fluid Dynamics, Gallery of Fluid Motion, November 21–23, 2010, Long Beach, California. Low Resolution Movie, High Resolution Movie, 2010.

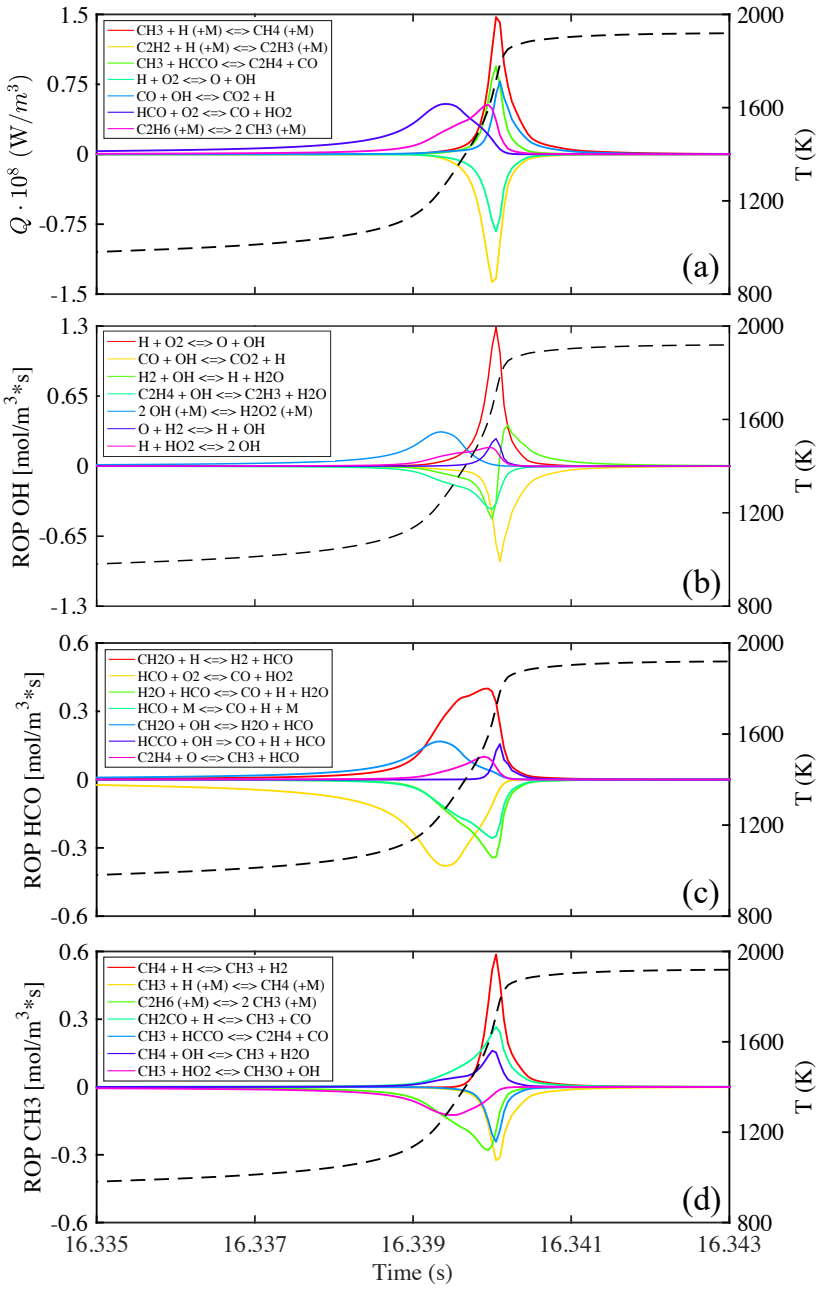

Figure 13: Heat release and rate of production (ROP) of OH, HCO, and CH_3 along the ignition particle for the top reactions during the second stage

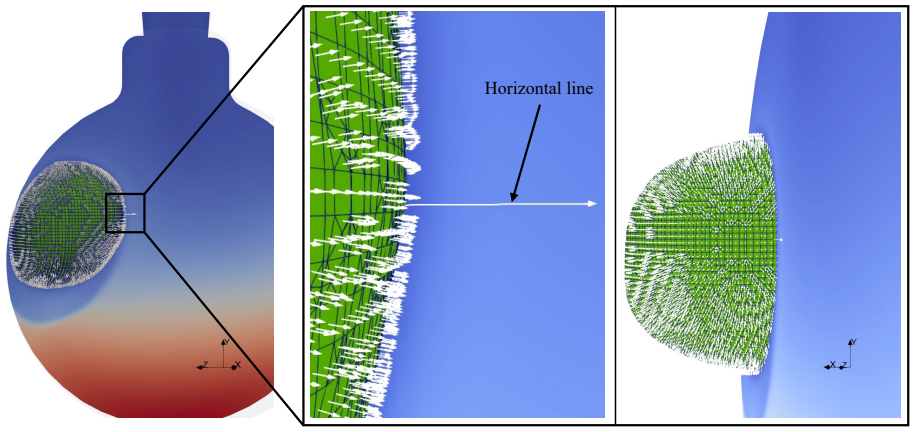

Figure 14: Flame front isosurface (T = 1500 K) with surface normal vectors and nC_6H_{14} mole fraction on a vertical cross-section through the flame. A horizontal line aligned with the flame propagation direction is shown

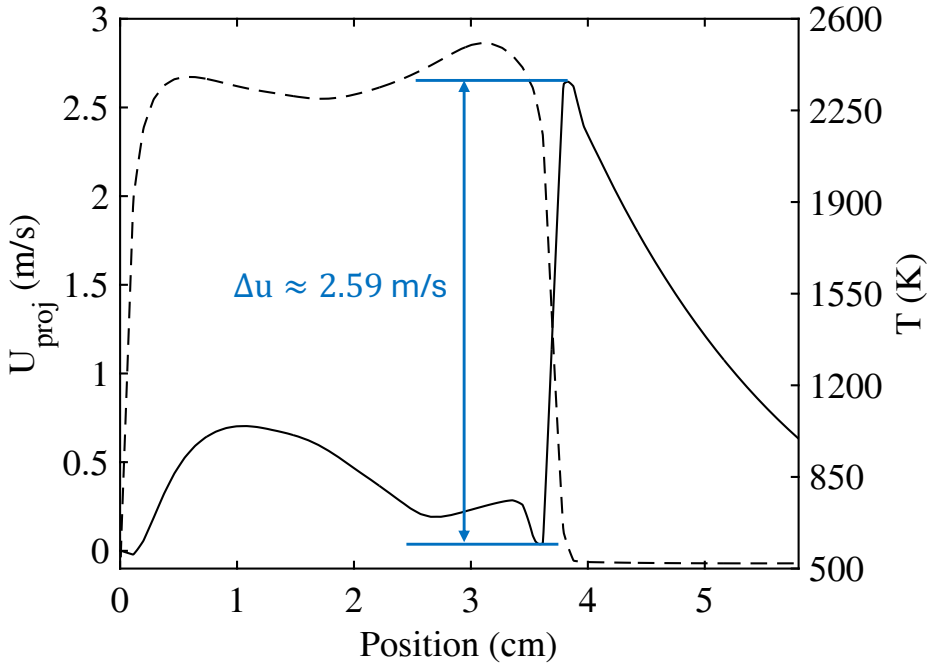

Figure 15: Projected velocity (-) and temperature (–) along the horizontal line across the flame front at height, y = 6.25 cm and time, t = 16.35065 s

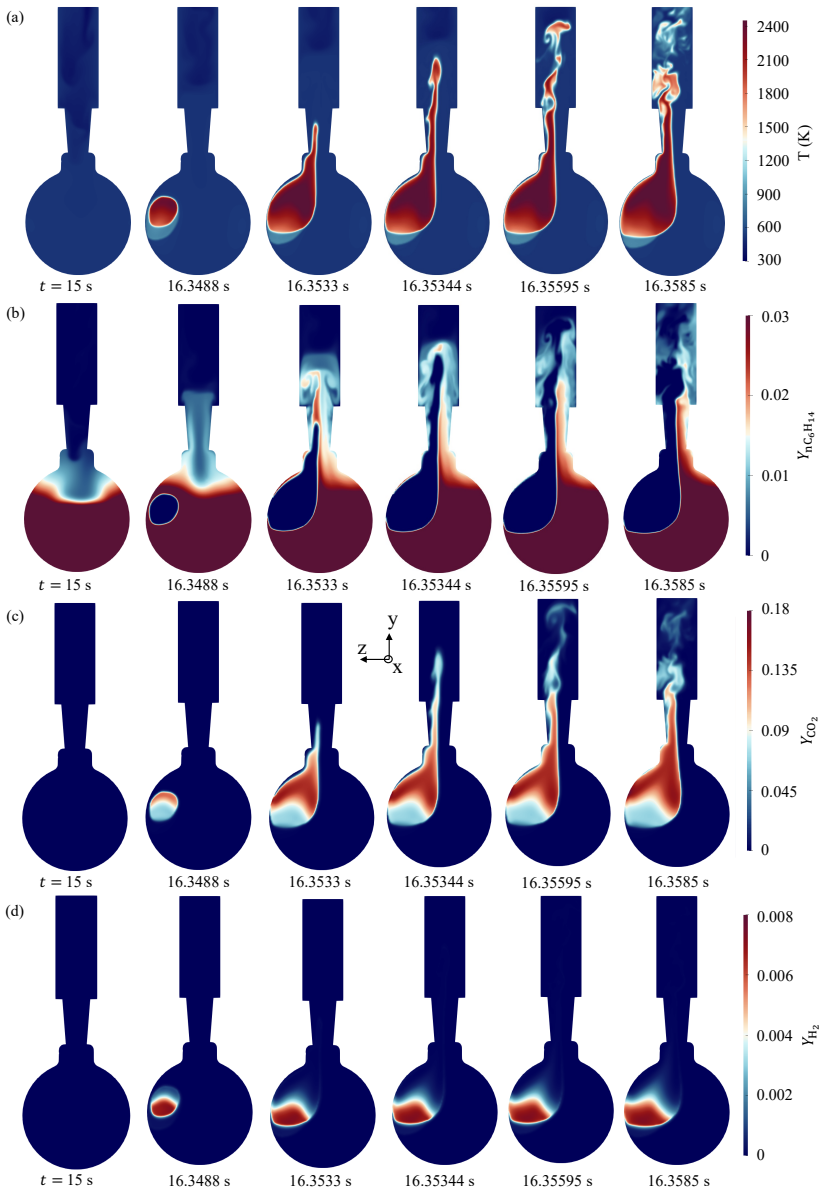

Figure 16: Flame evolution through the flask and holder along a vertical slice for (a) temperature, (b) colorbar-saturated nC_6H_{14} mass fraction to show fuel dispersion, (c) CO_2 mass fraction, and (d) H_2 mass fraction

Numerical Modeling of Gaseous n-Hexane Autoignition in an ASTM-E659 Apparatus

Branson Davis[a], Joseph Shepherd[a], Rémy Mével[b]

[a] *California Institute of Technology, Pasadena, 91125, CA, USA*
[b] *Zhejiang University, Hangzhou, China*

Supplemental Material

Experimental setup

For our study, the experimental setup used by [1] was adapted for the characterization of the AITs and additional thermocouple measurements at various locations in the flask were performed. This apparatus was constructed following the [2] standard. Figure 1 shows a picture and a cross-section drawing of the setup with the additional thermocouple locations illustrated.

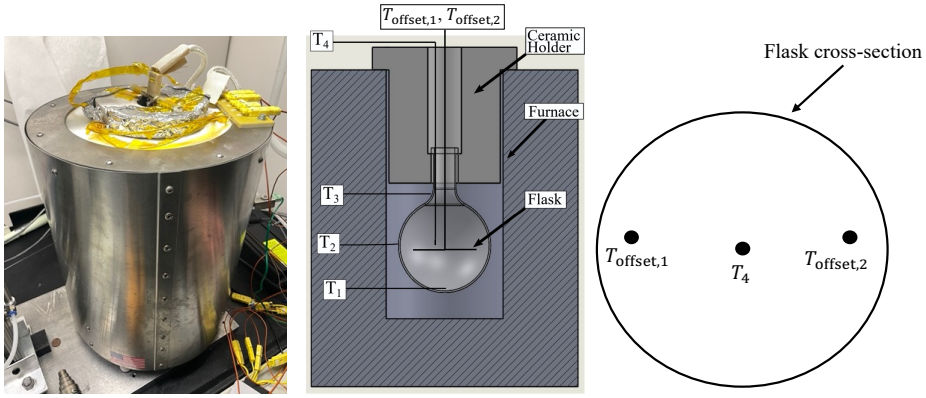

Figure S1: Experimental apparatus

The apparatus is composed of a Mellen CV12 crucible furnace with a 133 mm diameter and 200 mm deep cylindrical volume, which controllably heats

Email address: joseph.e.shepherd@caltech.edu (Joseph Shepherd)

a 500 mL round bottom, borosilicate flask up to 1250 °C with a PID controller (Love Controls series 16B) system accurate to ±1 °C. The flask is suspended in the furnace by a ceramic holder molded from silica-based Cotronics Rescor 750. The flask and ceramic holder are covered by aluminum foil to reflect the radiation inside the flask and reduce heat loss. The temperature of the flask surface is measured with three 34 gauge, type K thermocouples inside a mineral-insulated metal sheath, set at positions T_1, T_2, and T_3 (see Figure 1). A 36 gauge K-type thermocouple, T_4, was placed in the center of the flask to measure the air temperature.

Without good optical access, understanding where ignition occurs and how the flame propagates through the flask is difficult. To obtain more information, two additional bare-wire K-type 36 gauge thermocouples were inserted in the flask at the same height as T_4, but much closer to the walls. This was achieved by attaching the thermocouples to formed nitinol wire at 90° angles made with the vertical center line. Because of the "shape memory" property of nitinol to return to its preset austenite phase from its martensite phase upon heating, the nitinol/thermocouple assembly can be inserted into the flask folded up. Once heated, the two thermocouples extend outwards near the walls of the flask. This process is shown in Figure 2.

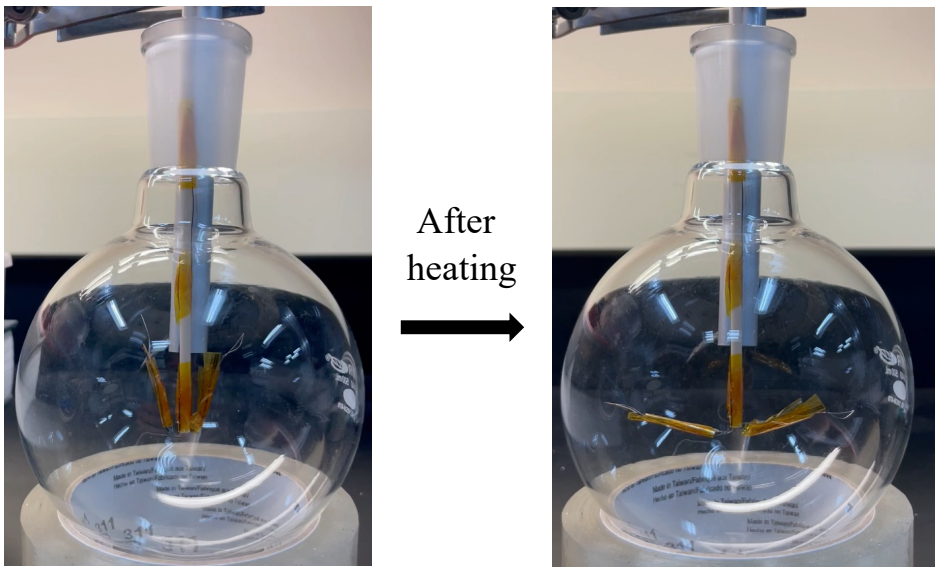

Figure S2: Two 36 gauge thermocouples attached to formed nitinol wire.

The temperature from the thermocouples are recorded with a NI 9213 16-channel, 24-bit, 75 Hz thermocouple data acquisition module from National Instruments, connected to a cDAQ-9171 CompactDAQ Chassis.

One-dimensional freely-propagating flame modeling

The resultant flame speed from the ignition event in the flask can be verified with well-resolved low-speed one-dimensional (1D) flame computations. In a flame-fixed coordinate system, the 1D freely propagating, premixed flame can be modeled assuming constant pressure with the steady-state equations for continuity, energy, and species in an infinite spatial dimension $-\infty < x < \infty$ as:

$$\frac{d(\rho u)}{dx} = 0\,, \tag{S1}$$

$$\rho u \frac{dY_i}{dx} = -\frac{d(\rho Y_i \boldsymbol{V}_i)}{dx} + \dot{\Omega}_i\,, \tag{S2}$$

$$\rho c_P u \frac{dT}{dx} = \frac{d}{dx}\big(\lambda \frac{dT}{dx}\big) - \rho \frac{dT}{dx} \sum_i^N c_{P,i} Y_i \boldsymbol{V}_i - \sum_i^N h_i \dot{\Omega}_i \tag{S3}$$

where ρ is the density, u is the velocity, c_P is the specific heat capacity at constant pressure, T is the temperature, and λ is the thermal conductivity. Y is the mass fraction, $\dot{\Omega}$ is the formation rate, h is the enthalpy, and $\boldsymbol{V}$ is the diffusion velocity. The subscript i denotes properties relating to species i and N is the total number of species.

Fickian diffusion was employed using mixture-averaged diffusion coefficients, D_i, calculated according to [3] as:

$$D_i = \frac{1 - Y_i}{\sum_{j \neq i}^N \frac{X_i}{\Gamma_{ji}}}\,, \tag{S4}$$

where Γ_{ji} are the binary diffusion coefficients. The diffusion velocity can then be calculated as:

$$\boldsymbol{V}_i = -\frac{D_i}{Y_i} \frac{dY_i}{dx}\,. \tag{S5}$$

The ideal gas equation of state was used to calculate the density of the mixture using the specific gas constant and mixture-averaged molecular weight.

Eqs. (S1)-(S3) are solved employing central differences with the following boundary conditions:

$$T(x = 0) = T_u\,, \tag{S6}$$

$$Y_i(x=0) = Y_{i,u}\,, \tag{S7}$$

$$\frac{dT}{dx}(x \to \infty) = 0\,, \tag{S8}$$

$$\frac{dY_i}{dx}(x \to \infty) = 0\,, \tag{S9}$$

where the subscript u represents the unburnt gas state. In practice, the solution is calculated on a finite domain $0 < x < L$ such that the spatial gradients at the boundary are ≈ 0. The model was implemented in Python based on Cantera's *adiabatic_flame.py* example code. The solution technique is a modified Newton's method to implicitly solve for u, T, ρ, Y_i, as well as the constant mass flux [4, 5]. Automatic grid refinement is carried out by first obtaining a solution on a coarse grid size, w, and then inserting point in regions with sharp temperature or species gradients (i.e., within the heat release zone of the flame). Typical converged grids had 100-200 cells across the flame for nC_6H_{14}/air mixtures. An example of the typical flame structure can be seen in Figure 3 which plots the primary species and temperature profiles across the flame front for an unburnt gas temperature, $T_u = 300$ K and a stoichiometric nC_6H_{14}/air mixture (equivalence ratio, $\phi = 1$) at 1 bar using the reduced *CaltechMech* mechanism described in Section 2.3. The position of the flame and domain size are arbitrary and depend on the solution scheme and grid refinement. Rapid oxidation of nC_6H_{14} into intermediates, such as C_2H_4 and CO, and finally into CO_2 by OH radicals can be seen across the flame.

With the unburnt u, and burnt, b, gas states, the flame propagates into the unburnt mixture at the laminar burning velocity, S_L, which can be computed from Eq. (S1). Since the mass flow rate is constant through the domain, $\rho_u S_L = \rho_b u_b$ and S_L can be calculated as:

$$S_L = \frac{\rho_b u_b}{\rho_u}\,. \tag{S10}$$

Of the many definitions of flame thickness, the most traditional definition is used to calculated ℓ_f according to [6] as

$$\ell_f = \frac{T_b - T_u}{\left(dT/dx\right)_{max}}\,. \tag{S11}$$

Eqs. S10 and S11 can be used to compute the laminar burning velocity and estimated flame thickness for a wide range of initial conditions. This

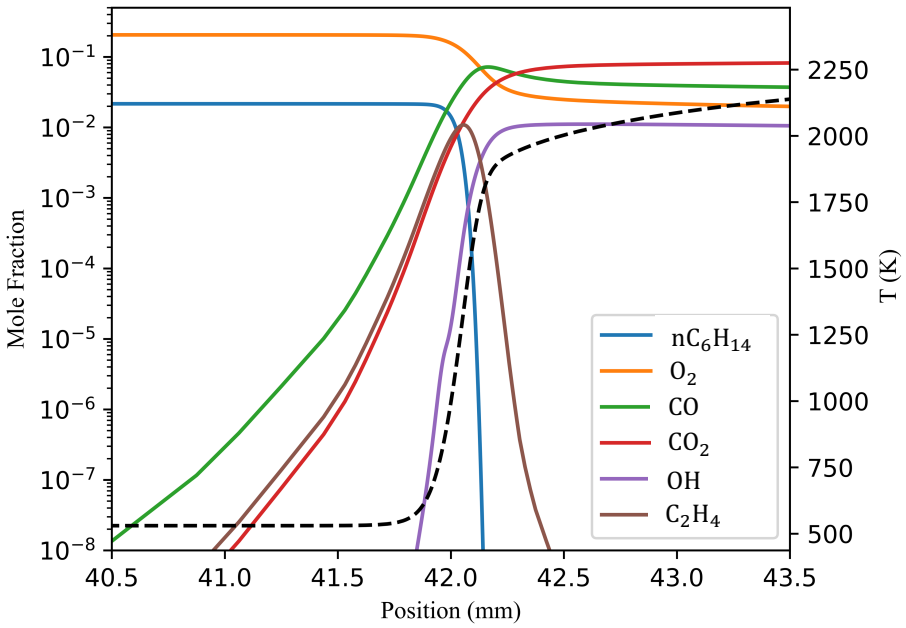

Figure S3: 1D flame model solution for $T_u = 300$ K and $\phi = 1$ at 1 bar using the reduced CaltechMech mechanism for a nC_6H_{14}/air mixture

technique is modified from the results presented by [7] to instead explore the low temperatures and wide range of equivalence ratios that exist in autoignition studies. The relevant unburnt gas temperatures were well below 930 K observed to have convergence issues [7]. Similarly, the equivalent ratio range was controlled to keep S_L much larger than 1 cm/s observed to also have convergence issues.

Figure 4 plots the solution surfaces for S_L (left) and ℓ_f (right) for 300 K $< T_u <$ 600 K and $0.5 < \phi < 1.9$ in nC_6H_{14}/air mixtures at 1 bar. The surfaces comprise approximately 1000 discrete simulations in the $\phi - T$ parameter space relevant to autoignition testing for nC_6H_{14}/air. A red line is traced along the surface at $T = 520$ K as this is approximately the temperature of the gas inside the flask for the present study. However, once the flame propagates out of the flask into the holder, gas temperatures down to nearly room temperature ($T \approx 300$ K) can exist. The black star on the laminar burning velocity plot corresponds to the condition used as verification for the 3D autoignition simulation. The inverse relation between S_L and ℓ_f can

be seen over the range of unburnt gas temperatures and equivalence ratios as discussed in [7]. For a fixed equivalence ratio, as the unburnt gas temperature is increased, the laminar burning velocity increased and the flame thickness decreased. For a fixed unburnt gas temperature, as the equivalence ratio is increased, S_L increases to a maximum and ℓ_f decreases to a minimum at $\phi = 1.1$. As ϕ continues to increase, S_L then decreases and ℓ_f increases again.

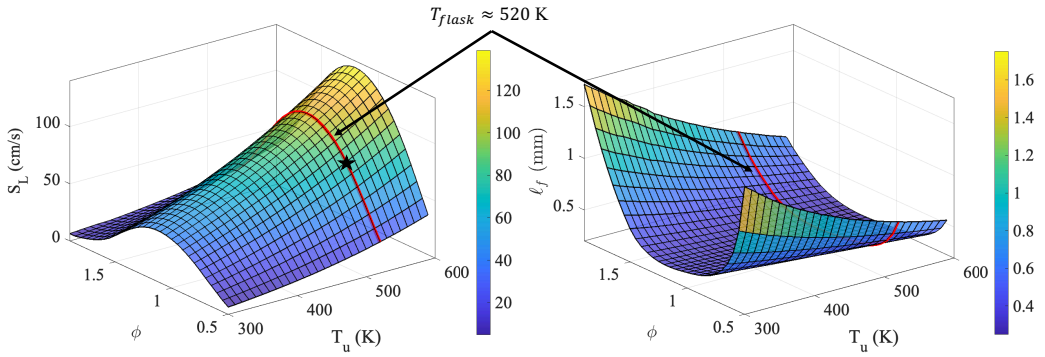

Figure S4: Computed S_L (left) and ℓ_k (right) surface maps for 300 K $< T_u <$ 600 K and $0.5 < \phi < 1.9$ for nC_6H_{14}/air mixtures at 1 bar. The red line illustrates approximate gas temperatures inside the flask and the black star indicates the approximate conditions compared to the 3D autoignition simulation

The S_L and ℓ_f curves presented in Figure 4 provide a useful first step for verifying the 3D flame propagation shown in the autoignition simulation.

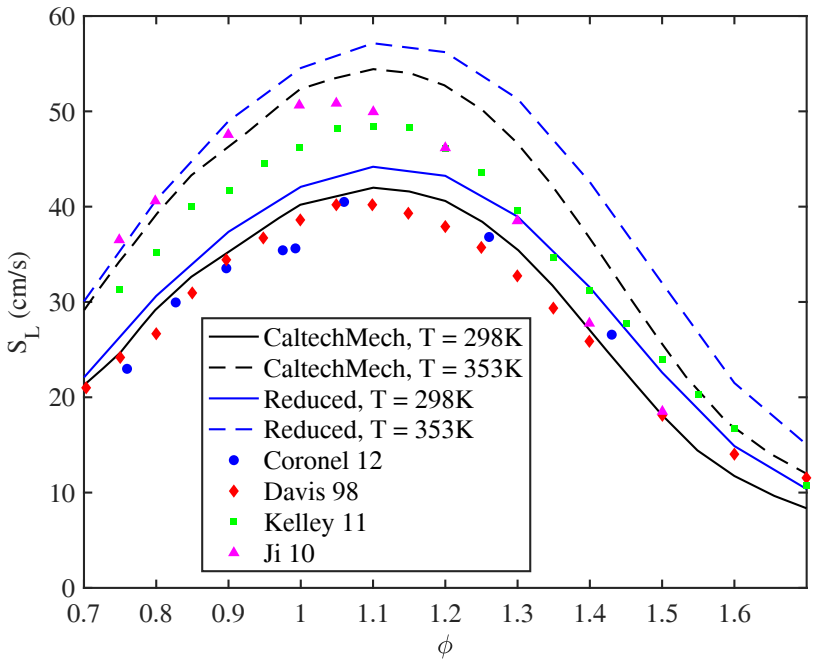

Figure S5: Comparison of the experimental and calculated laminar burning velocity for n-hexane-air mixtures

References

[1] C. D. Martin, J. E. Shepherd, Low temperature autoignition of jet a and surrogate jet fuel, J. Loss Prev. Process Ind. 71 (2021) 104454.

[2] ASTM-E659-24, Standard test method for autoignition temperature of liquid chemicals, American Society for Testing and Materials, 2024.

[3] C. F. Curtiss, J. O. Hirschfelder, Transport properties of multicomponent gas mixtures, J. Chem. Phys. 17 (1949) 550–555.

[4] D. G. Goodwin, H. K. Moffat, I. Schoegl, R. L. Speth, B. W. Weber, Cantera: An object-oriented software toolkit for chemical kinetics, thermodynamics, and transport processes, 2021. Version 2.5.1.

[5] S. P. M. Bane, Spark ignition: experimental and numerical investigation with application to aviation safety, Ph.D. thesis, California Institute of Technology, 2010.

[6] D. Spalding, V. Jain, The theory of steady laminar spherical flame propagation: Analytical solutions, Combust. Flame 5 (1961) 11–18.

[7] C. D. Martin, Experiments in Thermal Ignition: Influence of Natural Convection on Properties of Gaseous Explosions, Ph.D. thesis, California Institute of Technology, 2023.

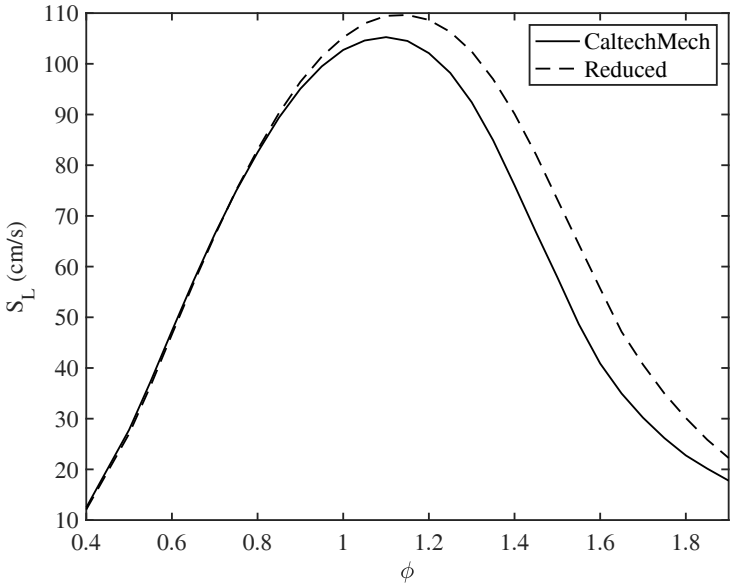

Figure S6: Calculated laminar burning velocity at $T = 520$ K and 1 bar for n-hexane-air mixtures

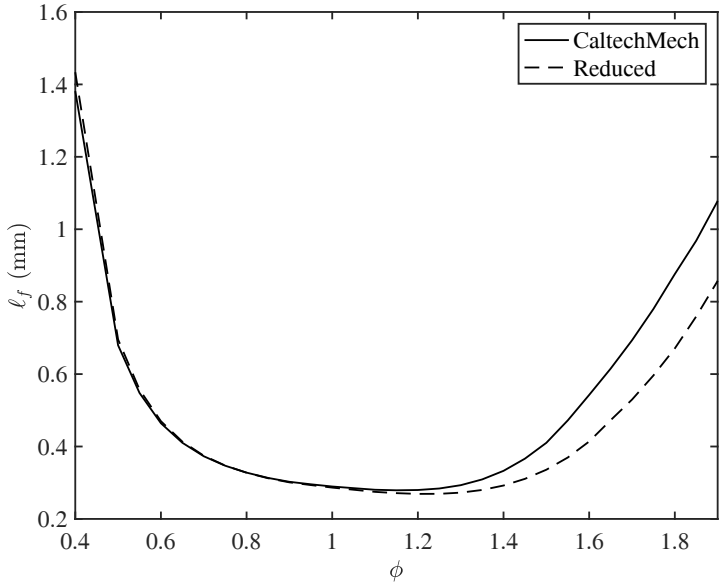

Figure S7: Calculated flame thickness at $T = 520$ K and 1 bar for n-hexane-air mixtures